

NIST Technical Note 2083

The Thermal Character of a 1 m Methanol Pool Fire

Kunhyuk Sung
Jian Chen
Matthew Bundy
Marco Fernandez
Anthony Hamins

This publication is available free of charge from:
<https://doi.org/10.6028/NIST.TN.2083>

NIST
**National Institute of
Standards and Technology**
U.S. Department of Commerce

NIST Technical Note 2083

The Thermal Character of a 1 m Methanol Pool Fire

Kunhyuk Sung
Jian Chen
Matthew Bundy
Marco Fernandez
Anthony Hamins
*Fire Research Division
Engineering Laboratory*

This publication is available free of charge from:
<https://doi.org/10.6028/NIST.TN.2083>

February 2020



U.S. Department of Commerce
Wilbur L. Ross, Jr., Secretary

National Institute of Standards and Technology
Walter Copan, NIST Director and Undersecretary of Commerce for Standards and Technology

Certain commercial entities, equipment, or materials may be identified in this document in order to describe an experimental procedure or concept adequately. Such identification is not intended to imply recommendation or endorsement by the National Institute of Standards and Technology, nor is it intended to imply that the entities, materials, or equipment are necessarily the best available for the purpose.

National Institute of Standards and Technology Technical Note 2083
Natl. Inst. Stand. Technol. Tech. Note 2083, 50 pages (February 2020)
CODEN: NTNOEF

This publication is available free of charge from:
<https://doi.org/10.6028/NIST.TN.2083>

TABLE OF CONTENTS

List of Tables	iii
List of Figures	iv
Abstract	vi
1. Introduction.....	1
2. Experimental Method.....	2
2.1. Pool Burner Setup.....	2
2.2. Thermocouple Temperature Measurements	3
2.3. Heat Flux Measurements	4
2.4. Flame Height and Pulsation Frequency	5
2.5. Liquid Fuel Temperature	6
3. Results and Discussion	7
3.1. Mass Burning Rate	7
3.2. Heat Release Rate	8
3.3. Flame Height and Pulsation Frequency	9
3.4. Temperature Distribution.....	9
3.5. Heat Flux Distribution	15
3.5.1. Radiative Fraction	17
3.6. Liquid Fuel Temperature Profile	21
4. Conclusions.....	22
5. References.....	23
Appendices.....	26
A. Thermal Properties	26
A.1. Thermochemical properties of methanol at =20 °C [18]	26
A.2. Thermophysical properties of a platinum thermocouple [16, 19].....	26
A.3. Thermophysical properties of air [18]	27
B. Bead temperature and gas temperature.....	28
C. Heat flux gauge information.....	29
D. Heat flux.....	30
D.1. Radial heat flux.....	30
D.2. Vertical heat flux	30
D.3. Radiative heat and Radiative fraction	30

E. Background Heat Flux Estimate	31
F. Uncertainty Analysis	34
F.1. Gas Temperature	34
F.2. Heat Flux	37
F.3. Radiative Fraction	37
G. Liquid Fuel Temperature	38
H. Cold Length of Thermocouple Wire	39
I. Plume Velocity Effect on Temperature Correction	40

List of Tables

Table 1. Measured mass burning rate in the 1 m methanol pool fire, heat release rate using the measured mass burning rate and from calorimetry. The uncertainty is expressed as the combined expanded uncertainty with a coverage factor of two, representing a 95 % confidence interval.....	8
Table 2. Comparison of the radiative fraction in steadily burning 30 cm and 100 cm methanol pool fires.	20
Table 3. Radiative fraction based on the single point estimate method at $r = 500$ cm with combined expanded uncertainty, representing a 95 % confidence interval.	21
Table A.1. Mean and variance of measured bead temperature and corrected gas temperature as a function of the axial and radial distance from the burner centerline.	28
Table A.2. Heat flux gauge locations from the burner centerline and calibration factor.	29
Table A.3. Mean and variance of radial heat flux as a function of the radial distance from the burner centerline.	30
Table A.4. Mean and variance of vertical heat flux as a function of the axial distance from the burner rim.	30
Table A.5. Radiative heat emitted from the fire and radiative fraction calculated by the integration method.	30
Table A.6. Initial and post background fluxes	31
Table A.7. Mean and variance of liquid fuel temperature as a function of the axial distance underneath the fuel surface. The radial position of the thermocouple is 35 cm from the burner centerline. U is the expanded uncertainty, representing a 95 % confidence interval.	38
Table A.8. Cold length and its variables as a function of temperature in $U_g = 2$ m/s, $d_w = 50$ μ m. The mean and variance of cold length is 0.94 mm \pm 0.02 mm.....	39
Table A.9. Mean and variance gas temperature in the axial centerline of burner rim using $U_g = 2$ m/s and $U_g = 5.5$ m/s.....	41

List of Figures

Figure 1. The round, 1 m diameter, water-cooled, steel burner with fuel level indicator and fuel overflow.	2
Figure 2. Image of thermocouple bead; units [μm].....	3
Figure 3. A schematic diagram of the heat flux gauge set-up.....	5
Figure 4. The RGB and binary images of the same frame.....	6
Figure 5. Instantaneous sequential digital images of the pulsing 1 m diameter methanol pool fire	7
Figure 6. Measured fuel mass on the load cell during Test 3. The fuel reservoir was refilled during periods indicated by the unshaded regions (except the furthest left region).	8
Figure 7. Fast Fourier power spectrum of the time-varying flame height.	9
Figure 8. Instantaneous temperature and time constant at $(z, r) = (30 \text{ cm}, 0 \text{ cm})$ during a 2.0 s period in Test 3; T_b is the bead temperature, T_r is the corrected temperature considering only radiative loss, T_g is the corrected gas temperature considering both radiation and thermal inertia effects.....	10
Figure 9. Time constant as a function of bead temperature with $U_g = 2 \text{ m/s}$ and $d_b = 150 \mu\text{m}$	11
Figure 10. Mean and variance of the bead temperature, corrected gas temperature and thermocouple time constant as a function of the axial distance above the burner along the centerline of the fire during Test 3.....	12
Figure 11. Mean and variance of gas temperature as a function of distance above the burner along the centerline of the fire.	12
Figure 12. Mean and variance of gas temperature as a function of radial position at various axial distances above the burner.	13
Figure 13. Ratio of the mean temperature (μ) to the standard deviation (σ) as a function of the mean temperature compared to previous results reported in 30 cm diameter methanol pool fires [4, 26]. 14	14
Figure 14. Mean and variance of the axial temperature profiles as a function of axial distance above the burner scaled by $Q^{2/5}$ and compared to previous results reported in 30 cm diameter methanol pool fires [4, 27, 28]. The horizontal error bars represent the uncertainty in $z/Q^{2/5}$ which is entirely due to the uncertainty in Q , which is dominated by measurement variance.	15
Figure 15. Mean and variance of heat flux as a function of; (a) radial distance from the burner centerline, (b) axial distance from the burner rim.....	16
Figure 16. Mean and variance of heat flux as a function of; (a) radial distance from the burner centerline, (b) axial distance from the burner rim, compared to the results of 100 cm methanol pool fire in Ref. [11]; variance of all heat flux outputs in Ref. [11] was 15%.....	16

Figure 17. (a) mean and variance of heat flux as a function of radial distance normalized by the pool diameter, (b) mean and variance of normalized heat flux as a function of axial distance normalized by the pool diameter, compared to the results of 7.1 cm, 30 cm and 100 cm methanol pool fire in Refs. [11, 29]. 17

Figure 18. Mean and variance radial radiative heat flux in the downward direction as a function of radial distance from the burner centerline at the plane defined by the burner rim ($z=0$)..... 19

Figure 19. Mean and variance vertical radiative heat flux as a function of axial distance above the burner for gauges facing the pool fire and 2.07 m from the centerline..... 19

Figure 20. Mean and variance of heat flux as a function of radial distance from the burner centerline with the gauge directed towards the fire. The error bars indicate the variance of the mean heat flux for gauges located 40 cm, 60 cm and 80 cm above the burner. 20

Figure 21. Mean and variance of fuel temperature as a function of the axial distance from the fuel surface in the pool fire test 1. The uncertainty in the temperature measurement is 2 °C [34]. 21

Figure A.1. Ambient temperature and cooling water temperature of gauges as a function of time during the experiment of Test 1. The yellow region indicates the average window..... 31

Figure A.2. Post background heat flux estimation for the gauge 12..... 32

Figure A.3. Uncorrected heat flux as a function of time and comparison of mean heat flux at $r=500$ cm in each gauge 33

Figure A.4 Reynolds number as a function of temperature in $U_g = 6$ m/s and $d_b = 150$ μ m..... 36

Figure A.5. Mean and variance of gas temperature as a function of the axial distance from the burner rim with $U_g = 2$ m/s and $U_g = 5.5$ m/s..... 40

Characteristics of a 1 m Methanol Pool Fire

Abstract*

A series of measurements were made to characterize the structure of a 1 m diameter methanol (CH₃OH) pool fire steadily burning with a constant lip height in a quiescent environment. The mass burning rate was measured by monitoring the mass loss in the methanol reservoir feeding the liquid pool. The heat release rate was measured using oxygen consumption calorimetry. Time-averaged local measurements of gas-phase temperature were conducted using 50 μm diameter, Type S, bare wire thermocouples, with a bead that was approximately spherical with a diameter of about 150 μm. The thermocouple signals were corrected for radiative loss and thermal inertia effects. The heat flux was measured in the radial and vertical directions and the radiative fraction was determined.

The average steady-state mass burning rate was measured as $12.8 \text{ g/s} \pm 0.9 \text{ g/s}$, which yields an idealized heat release rate of $254 \text{ kW} \pm 19 \text{ kW}$. The measured heat release rate was $256 \text{ kW} \pm 45 \text{ kW}$, which was consistent with the mass burning rate measurement. The maximum corrected mean and RMS temperature measured in the fire was $1371 \text{ K} \pm 247$, which occurred on the centerline, 30 cm above the burner rim. The results showed that the radiative fraction was $0.22 \pm 31\%$ in agreement with previous results.

KEYWORDS: heat release rate; temperature distribution; burning rate; heat flux distribution

* Certain commercial entities, equipment, or materials may be identified in this document in order to describe an experimental procedure or concept adequately. Such identification is not intended to imply recommendation or endorsement by the National Institute of Standards and Technology, nor is it intended to imply that the entities, materials, or equipment are necessarily the best available for the purpose.

1. Introduction

The focus of this study is to characterize the burning of a 1 m diameter pool fire steadily burning in a well-ventilated quiescent environment. Pool fires are a fundamental type of combustion phenomena in which the fuel surface is flat and horizontal, which provides a simple and well-defined configuration to test models and further the understanding of fire phenomena. In this study, methanol is selected as the fuel. Fires established using methanol are unusual as no carbonaceous soot is present or emitted. This creates a particularly useful testbed for fire models and their radiation sub-models that consider emission by gaseous species - without the confounding effects of blackbody radiation from soot.

Many studies have reported on the structure and characteristics of 30 cm diameter methanol pool fires, including the total mass loss rate [1-3], mean velocity [4], pulsation frequency [4] and gas-phase temperature field [4, 5]. With so many measurements characterizing the 30 cm methanol pool fire, it is a suitable candidate for fire modeling validation studies [3, 6-8]. On the other hand, research on the detailed structure and dynamics of larger pool fires is limited. Tieszen, *et. al.* [9, 10] used particle imaging velocimetry to measure the mean velocity field in a series of 1 MW to 3 MW methane and hydrogen pool fires burning in a 1 m diameter burner. Klassen and Gore [11] reported on flame height and the heat flux distribution near 1.0 m diameter pool fires burning a number of fuels including methanol. They used the same burner as this study, but with a 5 mm (rather than 10 mm as used here) lip height. . This study complements Ref. [11] by also measuring the local flame temperature throughout the flow field, the heat release rate using oxygen consumption calorimetry, and the radiative fraction determined by a single location measurement.

Use of fire modeling in fire protection engineering has increased dramatically during the last decade due to the development of practical computational fluid dynamics fire models and the decreased cost of computational power. Today, fire protection engineers use models like the Consolidated Fire and Smoke Transport Model (CFAST) and the Fire Dynamics Simulator (FDS) to design safer buildings, power plants, aircraft, trains, and marine vessels to name just a few types of applications [12, 13]. To be reliable, the models require validation, which involves a large collection of experimental measurements. An objective of this report is to provide data for use in fire model evaluation by the fire research community. Also, it is of interest to compare the burning characteristics of the 30 cm pool fire with the results presented here.

This report is broken into several parts. In Section 2, the experimental method and apparatus are described. The results are summarized in Section 3 and references are provided in Section 4. A series of appendices provide additional information. Appendix A provides information on the thermophysical properties of methanol as well as the temperature-dependent thermal properties of air and platinum used in the temperature measurement thermal inertia and radiative loss correction. Appendix B presents a table of the measured temperature and its corrected value. Appendix C provides details of the heat flux measurement. Appendix D lists the heat flux gauge calibration factors. Appendix E describes the background signal subtraction used in the heat flux measurement. Appendix F describes details of the uncertainty analysis for the gas temperature, heat flux, and radiative fraction determination. Appendix G describes liquid fuel temperature distribution.

2. Experimental Method

Steady-state burning conditions were established before measurements were initiated. A warm-up period of 10 min was required for the mass burning rate to be steady. Since back diffusion of water slowly accumulates in the fuel pool in methanol fires, fresh fuel was used between experiments. The purity of the methanol was 99.99 % by mass and the density was 792.7 kg/m^3 at $20 \text{ }^\circ\text{C}$, according to a report of analysis provided by the supplier. Experiments were conducted under an exhaust hood located 4 m above the burner rim. The effect of ambient convective currents on the fire was minimized by closing all inlet vents in the lab. The exhaust consisted of a large round duct (1.5 m diameter) located 6.0 m above the floor [14]. The smallest exhaust flow possible (about 4 kg/s) was used, helping to avoid perturbations (such as flame lean) and minimizing the influence of the exhaust on fire behavior. This led to the establishment of an unusually symmetric and recurring fire. The experiments were repeated three times.

2.1. Pool Burner Setup

A circular pan with an inner diameter (D) of 1.00 m, a depth of 0.15 m, and a wall thickness of 0.0016 m held the liquid methanol. An image of the burner is seen in Figure 1. The bottom of the burner was water-cooled. The burner was mounted on cinder blocks such that the burner rim was about 0.3 m above the floor. A fuel overflow basin included for safety extended 3 cm beyond the burner wall at its base. The fuel inlet was insulated and covered with a reflective foil to prevent preheating the fuel.



Figure 1. The round, 1 m diameter, water-cooled, steel burner with fuel level indicator and fuel overflow.

Fuel to the burner was gravity fed from a reservoir on a mass load cell raised 2 m above the floor and monitored by a data acquisition system. During these experiments, the level of the fuel was maintained 1 cm below the burner rim by regulating the fuel supply from the reservoir to the burner. The level was verified throughout the experiment by visually observing a video feed of the tiny tip of a sharpened (2 mm diameter) pointer that formed a barely discernable dimple on the fuel surface. The fuel level indicator is seen towards the left of the burner in Figure 1. A camera with optical zoom focused on the fuel level at the pointer, allowing observation of the fuel level. The uncertainty in the level was typically 3 mm.

2.2. Thermocouple Temperature Measurements

The local temperature was measured using a Type S (Pt 10% Rh/Pt), bare-wire, 50 μm fine diameter thermocouple. The selection of the diameter of a fine wire thermocouple must consider trade-offs between the durability of the instrument and measurement needs. The finer the wire, the smaller the radiative exchange with the environment and the faster the measurement time response, but the more fragile the thermocouple.

The thermocouple bead was approximately spherical as determined using an optical microscope. Figure 2 shows an image of the thermocouple bead, which was approximately spherical with an eccentricity of about 0.97. The bead diameter was approximately three times the wire diameter, or about 153.3 μm .

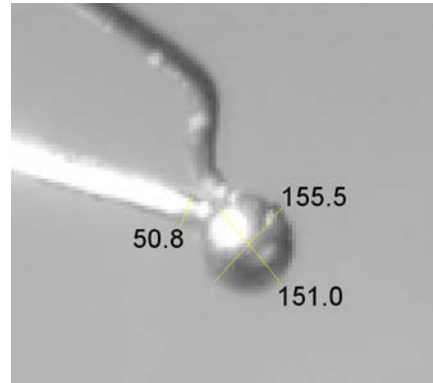


Figure 2. Image of thermocouple bead; units [μm].

A translation device was used to adjust the position of the thermocouple along a vertical axis aligned with the pool centerline. The vertical rail was aligned with the centerline of the burner and the S-type thermocouple was attached to the tip of a horizontal rod connected to the moving rail. The connection between the thermocouple and the rod was insulated and covered with aluminum foil to prevent heat-up. The measured signal was acquired at a rate of 60 Hz for 120 s, which represents about 170 flame puffing cycles.

The energy balance on the thermocouple bead considers convective and radiative heat transfer, which can be expressed as:

$$\dot{Q}_{conv} + \dot{Q}_{rad} = \rho_b \cdot c_{p,b} \cdot V_b \frac{dT_b}{dt} \quad (1)$$

where \dot{Q} is the net rate of heat transfer. ρ , $c_{p,b}$, and V_b are the density, specific heat and volume of the bead, respectively. Conductive heat transfer between the spherical bead and the lead wires is assumed to be negligible; the reason is explained in Appendix G.

If the response time of the thermocouple is larger than the fire fluctuation frequency, then thermocouple thermal inertial effects can impact the variance, although there is little influence on the mean [4]. The thermal inertial is related to the thermocouple time constant (τ), so the energy balance becomes:

$$T_g(t) = T_b(t) + \tau \frac{dT_b(t)}{dt} + \frac{\varepsilon\sigma}{h} (T_b^4(t) - T_{surr}^4) \quad (2)$$

$$\tau = \frac{m_b c_{p,b}}{hA_b} \quad (3)$$

where T_b is the bead temperature, T_g is the gas temperature, T_{surr} is the effective temperature of the surroundings, A_b is the surface area of the bead, σ is the Stefan-Boltzmann constant ($5.67 \cdot 10^{-8} \text{ W/m}^2/\text{K}^4$), and ε is the thermocouple emissivity. Here, the flame is taken as essentially optically thin based on estimates using the radiation subroutine in Ref. [6]. The convective heat transfer coefficient of gas flow near the bead is defined as $h = \text{Nu} \cdot \lambda_g / d_b$, where λ_g is the thermal conductivity of gas, d_b is the thermocouple bead diameter. In Eq. (2), the second and third terms of the right side represent the thermal inertial correction and radiation correction, respectively. The Nusselt number is empirically associated with the Reynolds and Prandtl numbers. The time constant for heat transfer to a sphere [15] can be written as:

$$\tau = \frac{\rho_b c_{p,b} d_b^2}{6\text{Nu}\lambda_g} \quad (4)$$

Following Shaddix [16], the Nusselt number for a sphere is calculated using the Ranz-Mashall model [17]:

$$\text{Nu} = 2.0 + 0.6 \text{Re}_d^{1/2} \text{Pr}^{1/3}; \quad 0 < \text{Re} < 200 \quad (5)$$

where Re is the Reynolds number and Pr is the Prandtl number. The temperature-dependent gas properties for Re and Pr , are taken as those of air [18], and the temperature dependent emissivity and the thermophysical properties of platinum were taken from [16, 19] which are listed in Appendix (A.2.); T_{surr} was assumed to be 300 K.

Solving Eq. (2) for T_g , the radiative correction for the gas temperature was found to be less than 30 K at the peak temperature (about 1800 K). Applying plume theory to calculate Re , the results showed that T_g had little sensitivity to the magnitude of the velocity for velocities between 2 m/s and 5 m/s. The results are described in Appendix I, which are consistent with the results of Shaddix [16]. The combined expanded uncertainty (representing a 95 % confidence interval) in the temperature measurement was estimated as 66 % on-average, which was almost entirely due to measurement variance. Unless otherwise noted, the uncertainty reported in this paper is the combined uncertainty representing a 95 % confidence interval with a coverage factor of 2 [20].

2.3. Heat Flux Measurements

The radiative heat flux emitted to the surroundings was measured using a wide-view angle, water-cooled, Gardon-type total heat flux gauges with 1.3 cm diameter faces. Fourteen gauges were used to measure the heat flux distribution about the pool fire as shown in Figure 3. Radial heat flux gauges were aligned along the plane of the burner rim to measure the heat flux in the downward direction. Vertical heat flux gauges were aligned to measure the heat flux in the radial direction away from the fire. In addition,

Gauges 12 to 14 were moved horizontally in the radial direction, using a computer-controlled mechanical traverse. The heat flux measurement positions are listed in Appendix D.

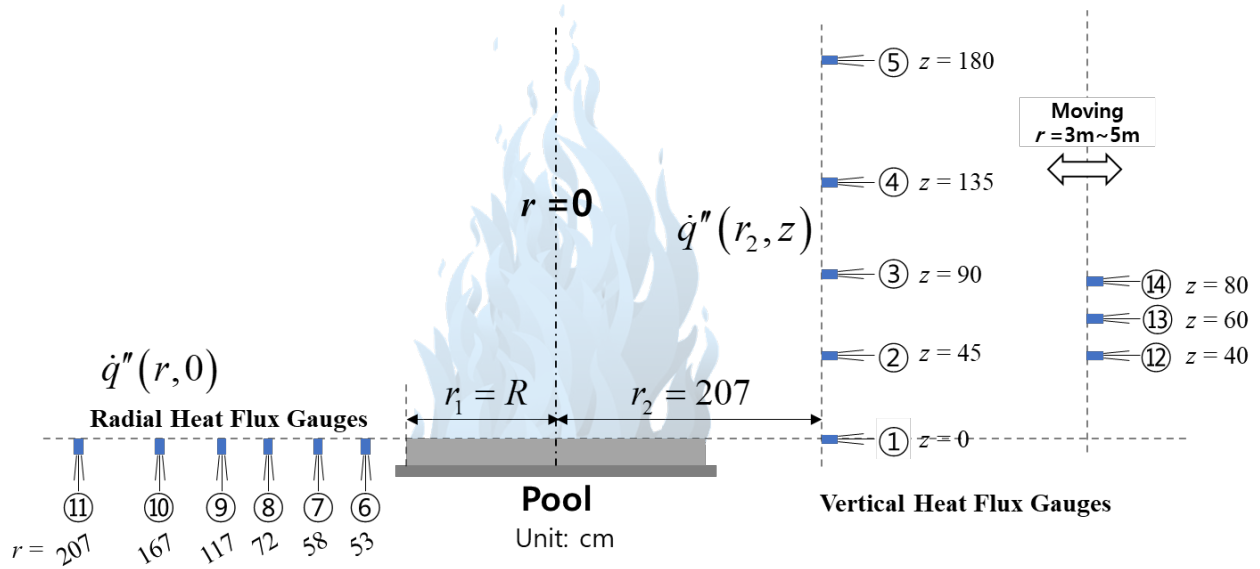


Figure 3. A schematic diagram of the heat flux gauge set-up.

2.4. Flame Height and Pulsation Frequency

A 30 Hz video record of the fires was used to determine the flame height and the dominant pulsation frequency. About 3600 frames, representing roughly 170 puffing cycles, in the video record were analyzed by MATLAB to determine the flame height.

The video record of flame appearance was decompressed into RGB images. In these images, the flame region could be distinguished from the background by the value of Blue. Based on the threshold of Blue values as suggested by Otsu [21], the images were transformed into binary images. The RGB and binary images of the same frame are shown in Figure 4.

The instantaneous flame height was defined as the distance between the burner and flame tip and the mean flame height (Z_f) was defined as the distance between the pool surface and the flame surface when the intermittency is 0.5 [22]. A fast Fourier transform was applied to the transient flame height to determine the dominant puffing frequency.

The experimental measurements are compared to flame height correlations from the literature. Heskestad [22] developed a correlation for flame height (Z_f) as follows:

$$\frac{Z_f}{D} = 15.6N^{1/5} - 1.02 \quad (6)$$

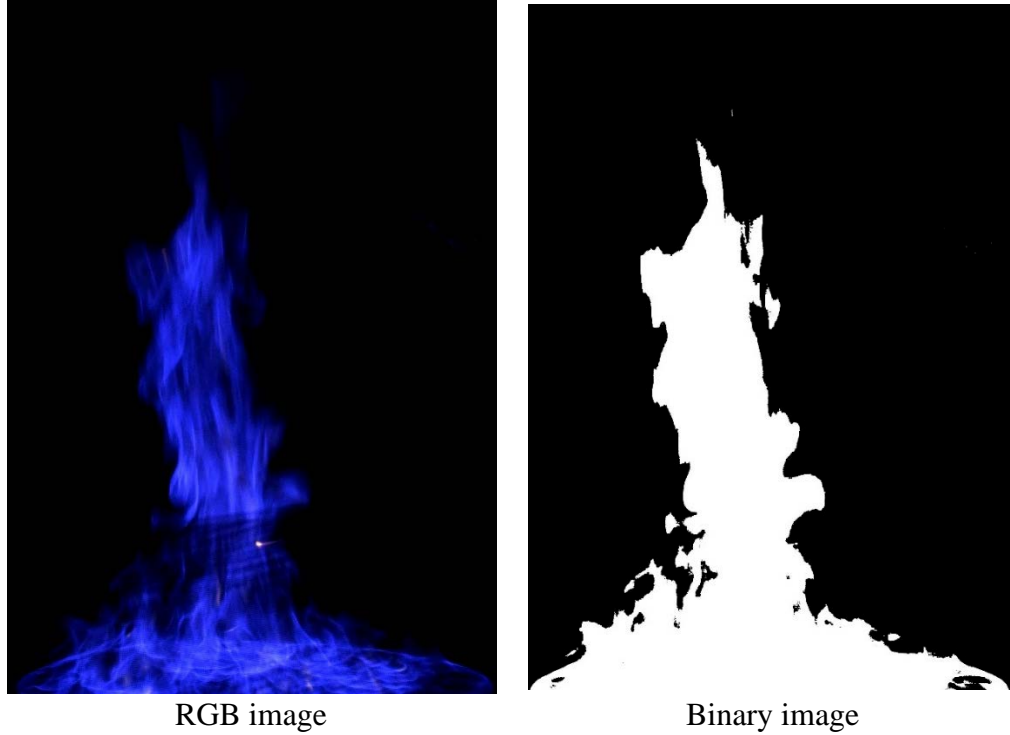


Figure 4. The RGB and binary images of the same frame.

where the nondimensional number N is defined as:

$$N = \left[\frac{c_p T_0}{g \rho_0^2 (H_c / \gamma)^3} \right] \frac{\dot{Q}^2}{D^5} \quad (7)$$

where c_p , T_0 , g , ρ_0 , H_c , γ , D and \dot{Q} are the specific heat, environmental temperature, gravitational acceleration, ambient density, the heat of combustion, the mass-based stoichiometric air-to-fuel ratio, the pool fire diameter, and heat release rate, respectively.

2.5. Liquid Fuel Temperature

A manually adjustable vertical mount was used to measure the vertical temperature distribution in the liquid fuel. A ½ mm diameter bare-bead K-type thermocouple was attached to the tip of the vertical mount and the vertical position was monitored with a strain gauge shielded with aluminum foils to prevent heat transfers from the fire. The radial position of the thermocouple was fixed at $r = 35$ cm, and the thermocouple was moved vertically in the range from -5 cm to 1 cm below the fuel surface. Temperature data were acquired for 30 s at each position at 1 Hz sampling rate. The measurement was repeated twice at 10 minutes and 45 minutes after the fire ignition in the steady fire conditions.

3. Results and Discussion

The shape of the fire dramatically changed during its pulsing cycle. The fire was blue with no indication of the presence of soot. The observed dynamic fire shape is consistent with the careful description given by Weckman and Sobiesiak [23] for a medium-scale acetone pool fire and with the analysis given by Baum and McCaffrey [24]. Figure 5 shows four sequential images of the pulsing methanol pool fire. A series of repeated cycles in which orderly curved flame sheets anchored at the burner rim were connected to the central fire plume and rolled towards the fire centerline, necked-in to form a narrow and long visible fire plume.

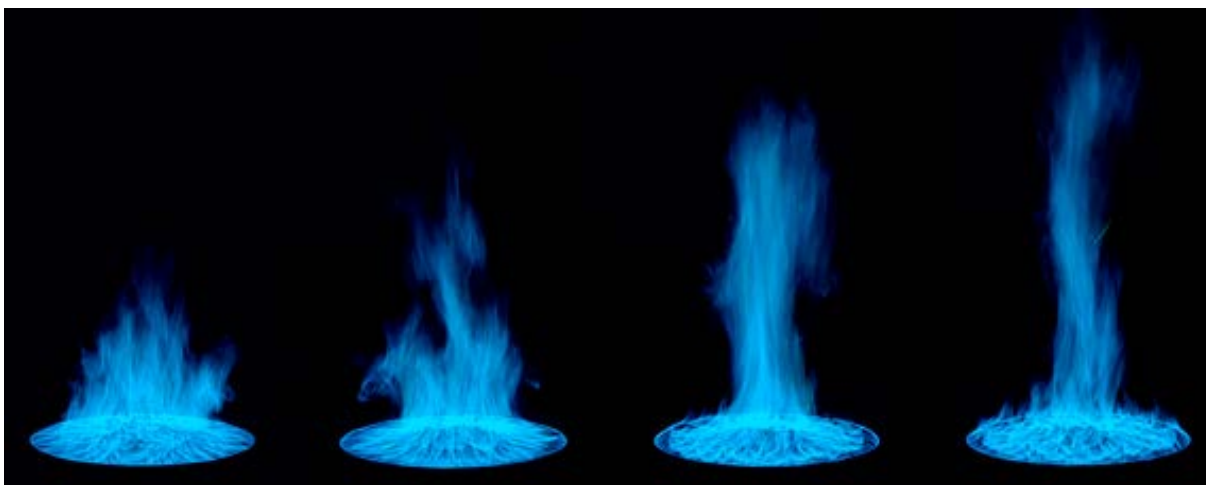


Figure 5. Instantaneous sequential digital images of the pulsing 1 m diameter methanol pool fire

3.1. Mass Burning Rate

The mass burning rate was measured by monitoring the mass loss in the 20 L methanol reservoir feeding the liquid pool, using a calibrated load cell. Figure 6 shows the time-varying fuel mass during Test 3. When the fuel level was low in the reservoir, it needed to be replenished. The periods when the reservoir was refilled are indicated by the white (unshaded) regions in Figure 6. During these periods, the fuel was still fed to the burning pool and the fuel level in the pool was maintained constant as verified by a video camera focused on the relative level of the fuel compared to the fuel level indicator (see Figure 1). The burning rate is estimated during the gray regions in the figure, that is, after an initial warm-up and avoiding periods when fuel was added to the reservoir. The total mass loss rate for each period is noted (by the numbers in the gray regions) by considering the ratio of the mass loss to the duration of the period. The time-weighted average mass burning rate during the three experiments was $12.8 \text{ g/s} \pm 0.9 \text{ g/s}$, where the uncertainty represents the combined uncertainty representing a 95 % confidence interval.

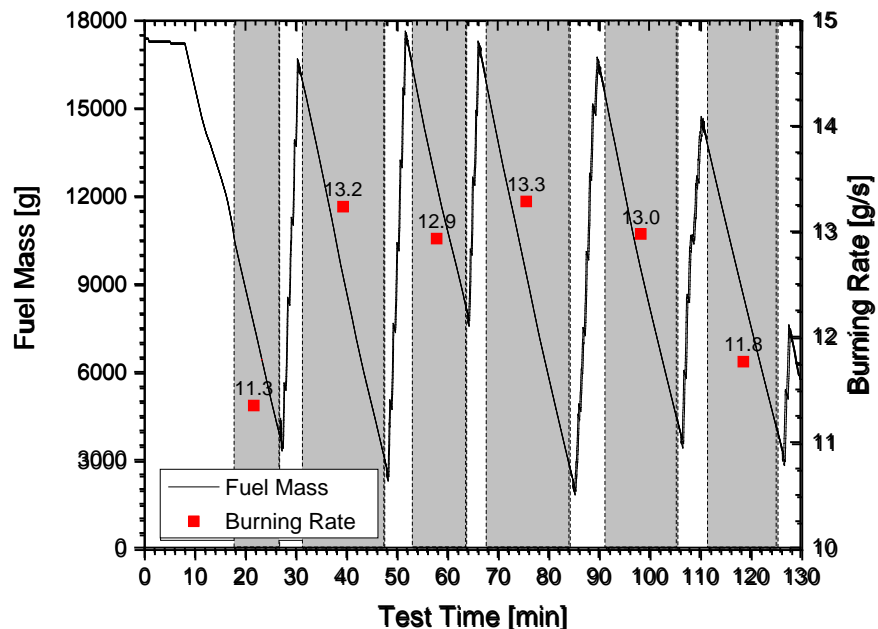


Figure 6. Measured fuel mass on the load cell during Test 3. The fuel reservoir was refilled during periods indicated by the unshaded regions (except the furthest left region).

3.2. Heat Release Rate

The heat release rate was measured using oxygen consumption calorimetry and compared with the ideal heat release rate (\dot{Q}) calculated from the mass burning rate, i.e., $\dot{m}\Delta H_c$ where ΔH_c is the net heat of combustion of methanol – equal to 19.9 kJ/g [18]. The heat release rate from calorimetry was averaged for the three tests once the fire reached steady-state burning.

The measured mass burning rate, the ideal heat release rate, and heat release rate measured via the oxygen consumption calorimetry are presented in Table 1. As expected, the ideal heat release rate agrees well with the measured calorimetric heat release rate since the combustion efficiency is expected to be nearly 1.0. The expanded uncertainty of heat release rate measurement using the calorimetry was 7 % based on repeat measurements, the results and methods described in [14], and additional natural gas calibrations at 250 kW. The heat release rate from the calorimetry was 256 kW \pm 45 kW.

Table 1. Measured mass burning rate in the 1 m methanol pool fire, heat release rate using the measured mass burning rate and from calorimetry. The uncertainty is expressed as the combined expanded uncertainty with a coverage factor of two, representing a 95 % confidence interval.

Mass burning rate \dot{m} [g/s]	Ideal Heat Release \dot{Q} [kW]	Heat Release Rate from calorimetry \dot{Q}_a [kW]
12.8 \pm 0.9	254 \pm 19	256 \pm 45

3.3. Flame Height and Pulsation Frequency

The mean flame height was measured as 1.10 m with a standard deviation of 0.22 m. Using Eq. (6), with $\gamma=6.47$, $D = 1$ m, and $\dot{Q} = 256$ kW, the flame height was calculated as 1.16 m, in agreement with the measured value. Calculating the fast Fourier transform of the transient value of the flame height, the relationship between frequency and amplitude is shown in Figure 7. The dominant frequency of the pool fire was about 1.37 Hz consistent with previous studies [25]. The first harmonic of the dominant frequency is also evident, exemplifying the repetitive and coherent nature of this pulsing fire.

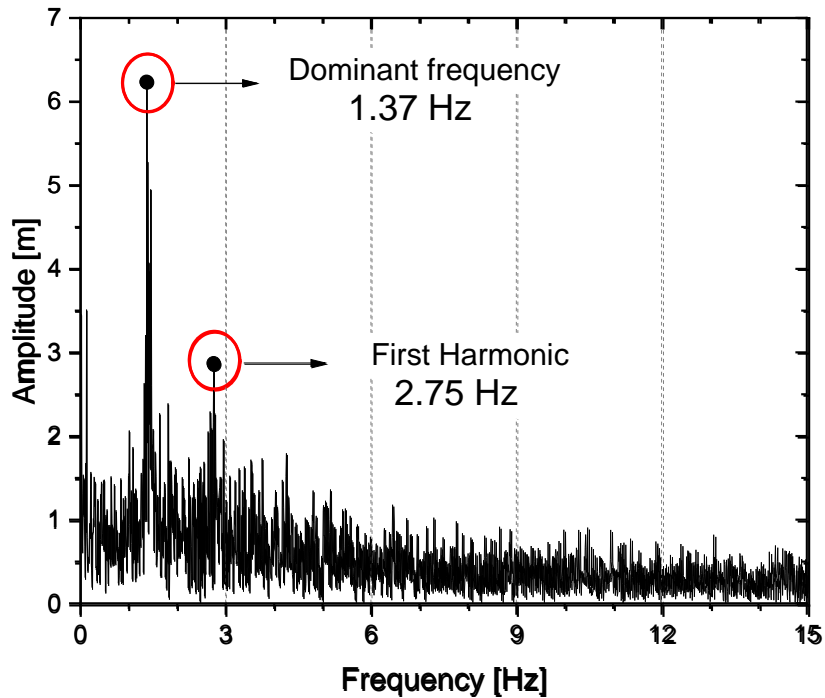


Figure 7. Fast Fourier power spectrum of the time-varying flame height.

3.4. Temperature Distribution

Figure 8 shows 2.0 s of the time series of the measured bead temperature (T_b), the radiation corrected temperature (T_r) considering only the radiation correction term (not thermal inertia) in Eq. (2), and the radiation and inertia corrected gas temperature (T_g).

There was no phase-delay between the bead temperature (T_b) and the radiation corrected temperature (T_r). The radiation correction ($T_r - T_b$) became larger as the bead temperature increased with the correction equal to 7 K for $T_b = 1070$ K and about 54 K for $T_b = 1730$ K, which was the highest instantaneous temperature.

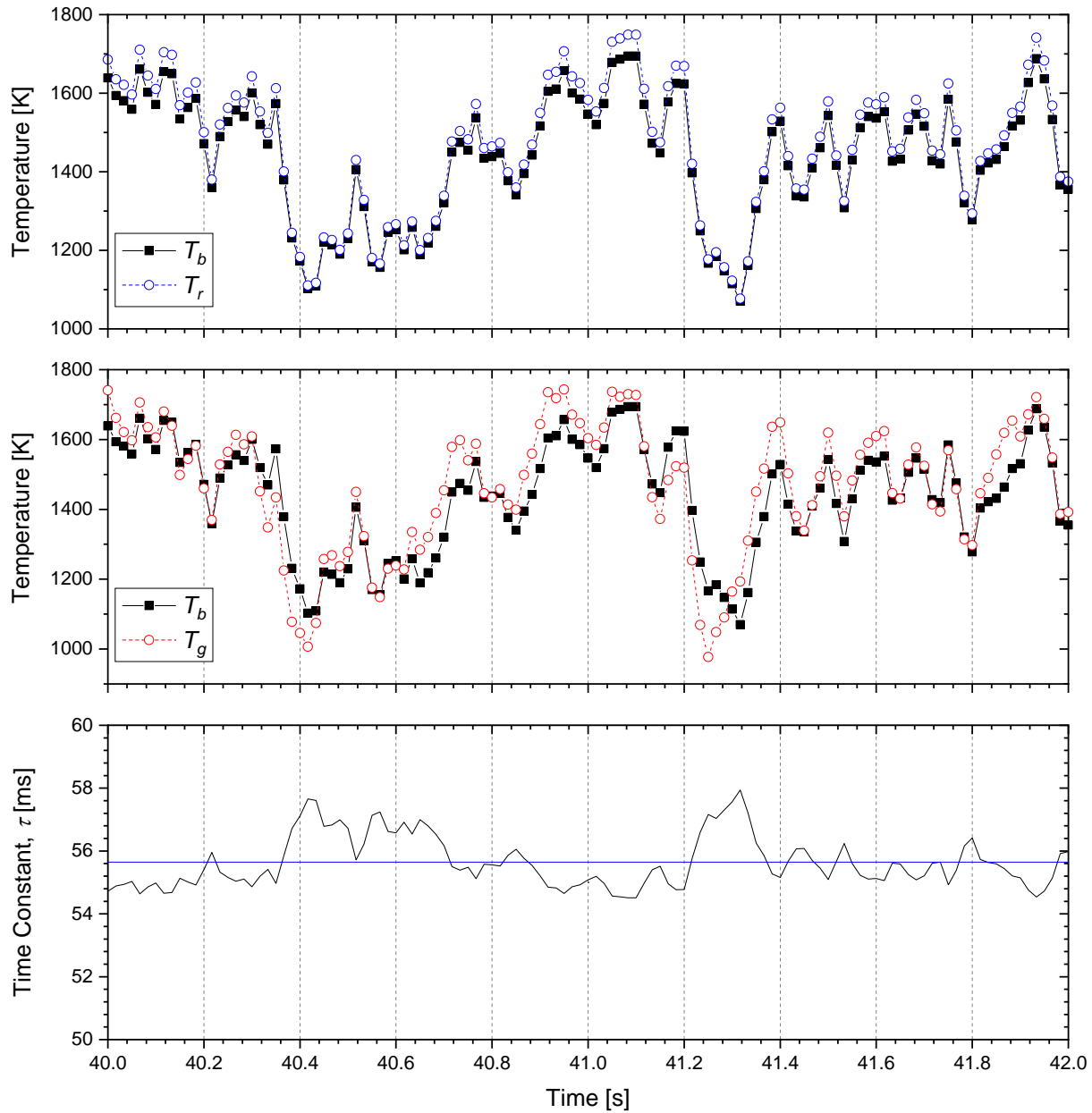


Figure 8. Instantaneous temperature and time constant at $(z, r) = (30 \text{ cm}, 0 \text{ cm})$ during a 2.0 s period in Test 3; T_b is the bead temperature, T_r is the corrected temperature considering only radiative loss, T_g is the corrected gas temperature considering both radiation and thermal inertia effects.

Solving Eq. (2) for T_g , the sum of the correction terms was found to be less than 60 K near the peak temperature. Thermal inertia caused a time delay for T_g following T_b , particularly when the temporal temperature gradient was large. The corrected peak gas temperature was typically about 100 K lower than the associated peak bead temperature. The minimum correction was 7 K for $T_b = 1070 \text{ K}$ at 41.3 s. The corrected gas temperature was 190 K lower than the bead temperature at 41.2 s, whereas it was 155 K higher than the bead temperature at 41.9 s.

The time constant changed inversely with the temperature variance as seen in Figure 8. The mean time constant was calculated as $56 \text{ ms} \pm 17 \text{ ms}$ where the uncertainty represents a propagation of error analysis of Eq. (4). Figure 9 shows the time constant as a function of the bead temperature with $U_g = 2 \text{ m/s}$ and $d_b = 150 \text{ }\mu\text{m}$. Calculating Eq. (4) assuming the properties of air, the time constant decreased from 68 ms to 53 ms (a 22 % decrease) as the air temperature increased from 400 K to 1800 K.

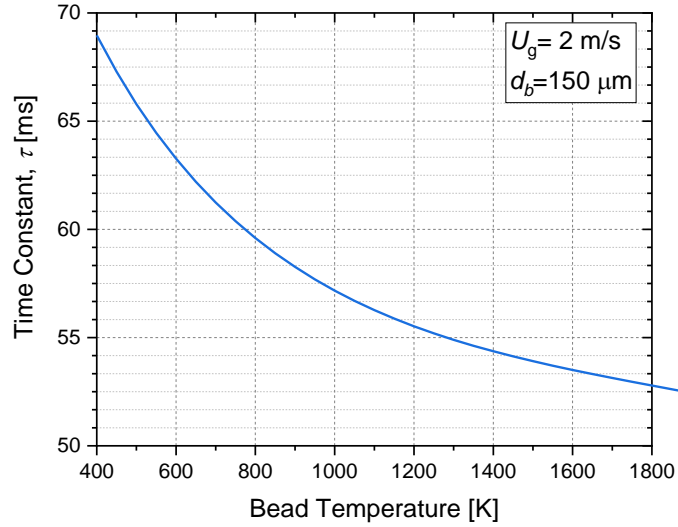


Figure 9. Time constant as a function of bead temperature with $U_g = 2 \text{ m/s}$ and $d_b = 150 \text{ }\mu\text{m}$.

Figure 10 shows the mean and variance of the bead temperature (T_b), the corrected gas temperature (T_g), and the calculated time constant as a function of distance above the burner along the centerline of the fire during Test 3. As expected, the mean gas temperatures were slightly larger than the mean bead temperature for all positions. The mean time constant changed inversely with the mean gas temperature, in agreement with the results in Figure 9.

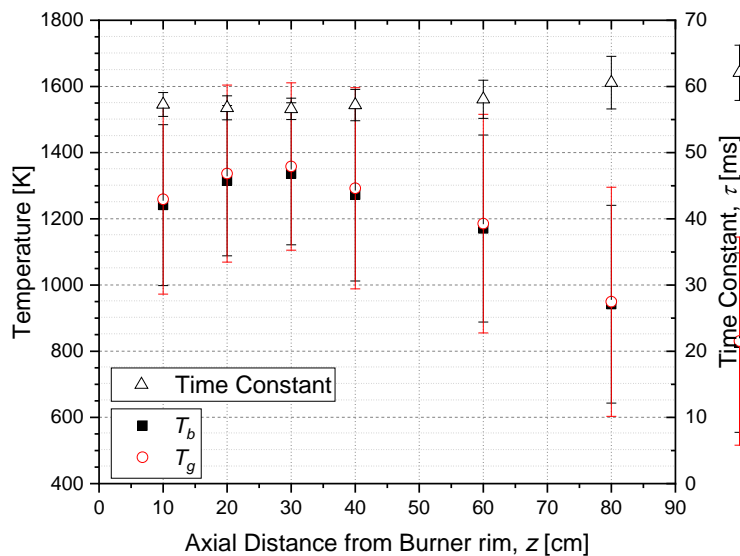


Figure 10. Mean and variance of the bead temperature, corrected gas temperature and thermocouple time constant as a function of the axial distance above the burner along the centerline of the fire during Test 3.

Figure 11 shows the corrected gas temperature as a function of distance above the burner along the centerline. The maximum corrected temperature was 1370 K, which occurred about 0.30 m above the burner. The gradient near the fuel surface in Figure 11 was steep. At 0.05 m above the burner, the gas temperature was about 1141 K \pm 296 K. The temperature at the fuel surface was measured to be at the boiling point of methanol, 338 K, yielding a temperature gradient near the fuel surface of about 160 K/cm \pm 60 K/cm (see discussion in Section 3.6).

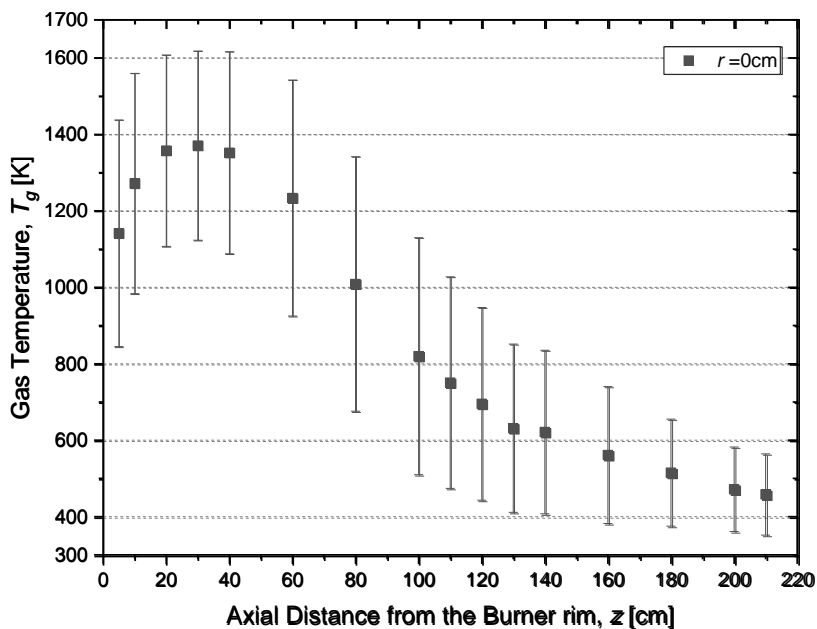


Figure 11. Mean and variance of gas temperature as a function of distance above the burner along the centerline of the fire.

Figure 12 shows the mean and variance of the corrected gas temperature in the radial direction as a function of axial distance above the burner ($20 \text{ cm} \leq z \leq 180 \text{ cm}$). The mean temperature decreased steeply at $z \geq 10 \text{ cm}$. The maximum temperature occurs near the centerline for each elevation demonstrating the symmetry of the fire. The gradient diminished with the axial distance away from the fuel surface. Appendix B presents a table of the measured bead and corrected gas temperatures, and Appendix F.1 describes details of the temperature measurement uncertainty analysis.

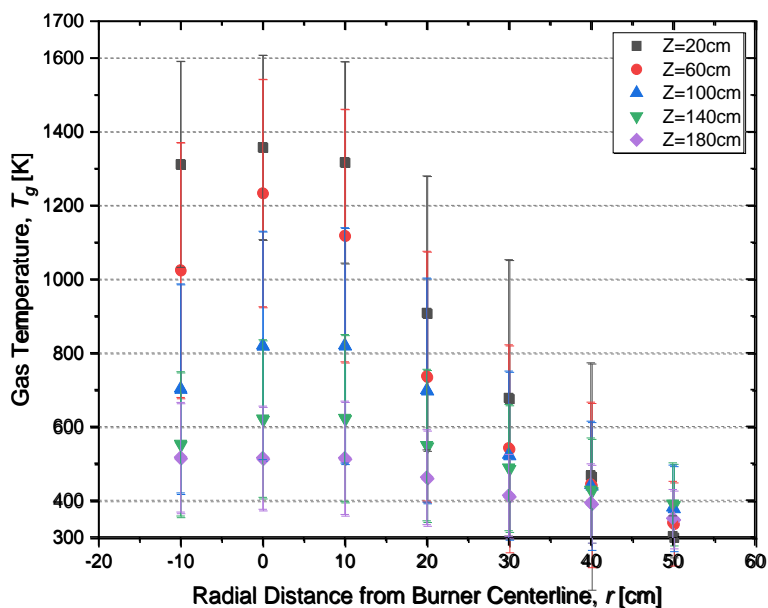


Figure 12. Mean and variance of gas temperature as a function of radial position at various axial distances above the burner.

Figure 13 shows the ratio of mean temperature and standard deviation as a function of mean temperature. The ratio decreased until about 750 K, then increased continuously as the mean temperature increased. These results suggest that methanol pool fires are highly structured with temperature fluctuations larger in high and low temperature fire regions.

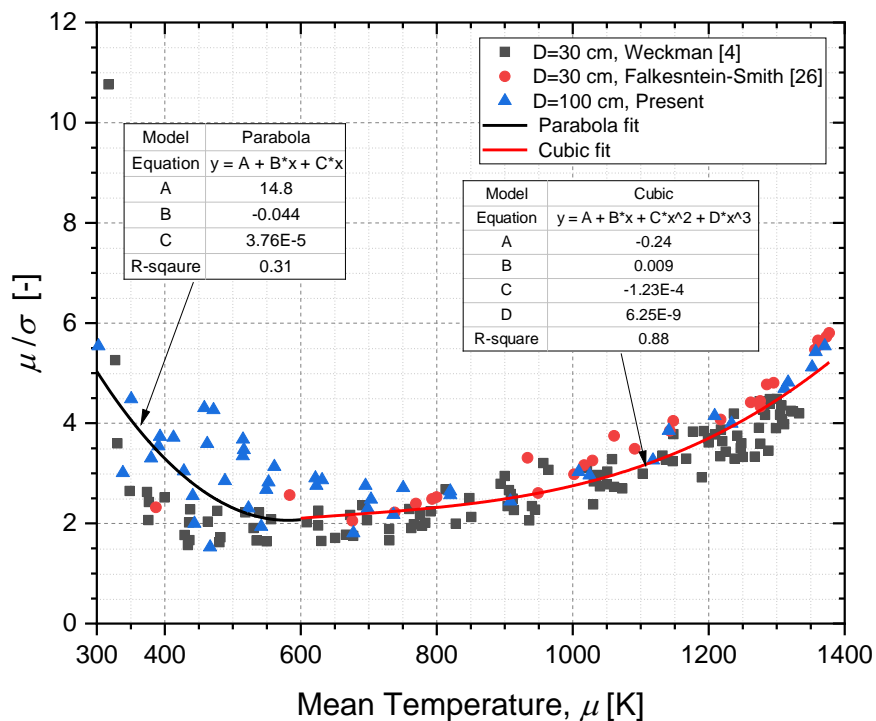


Figure 13. Ratio of the mean temperature (μ) to the standard deviation (σ) as a function of the mean temperature compared to previous results reported in 30 cm diameter methanol pool fires [4, 26].

Figure 14 shows the mean and variance of the axial temperature profile as a function of scaled axial distance. The results are compared to previous measurements in 30 cm diameter methanol pool fires from Refs. [4, 27, 28]. Axial distance above the burner is scaled by $\dot{Q}^{2/5}$ following Baum and McCaffrey [24]. Weckman and Strong [4] measured temperature in a 30.5 cm diameter methanol pool fire with a rim height of 1 cm using a 50 μm wire diameter, bare bead, type S (Pt 10% Rh/Pt), the thermocouple is similar to the thermocouples used in this study. The measurements of Hamins and Lock [27] are also shown, where the temperature was measured using a 75 μm wire diameter, bare bead, Type S thermocouple in a steadily burning 30.1 cm diameter methanol pool fire with a 0.6 cm lip. The radiation corrected thermocouple measurements in Ref. [28] are also shown, which used a 50 μm wire diameter, bare bead, Type S thermocouple in a steadily burning 30.1 cm diameter methanol pool fire with a 1 cm lip. A comparison of the results presented in Figure 14 shows that the 1 m and 30 cm pool temperatures track each other within experimental uncertainty.

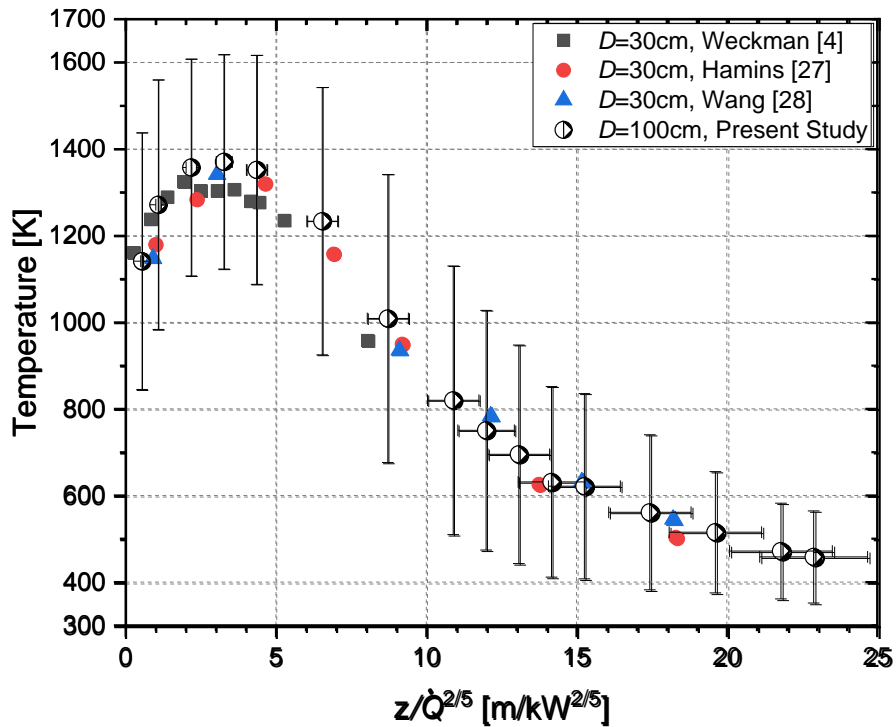


Figure 14. Mean and variance of the axial temperature profiles as a function of axial distance above the burner scaled by $\dot{Q}^{2/5}$ and compared to previous results reported in 30 cm diameter methanol pool fires [4, 27, 28]. The horizontal error bars represent the uncertainty in $z/\dot{Q}^{2/5}$ which is entirely due to the uncertainty in \dot{Q} , which is dominated by measurement variance.

3.5. Heat Flux Distribution

Figure 15 shows the mean radial radiative heat flux as a function of the radial and axial distances from the burner. As expected, the radiative heat flux rapidly decreases with distance from the centerline. The maximum radial heat flux was $5.1 \text{ kW/m}^2 \pm 1.0 \text{ kW/m}^2$. The heat flux decreased consistently proportional to $1/r^2$ as seen in the figure. There was little change in the radiative heat flux in the axial direction. The heat flux has a maximum value of $1.0 \text{ kW/m}^2 \pm 0.1 \text{ kW/m}^2$ at 0.9 m height above the burner. Appendix C lists the calibration factor of heat flux gauges. Appendix D provides tables with the values of the heat flux measurements. Appendix E describes the background signal subtraction used in the heat flux measurement.

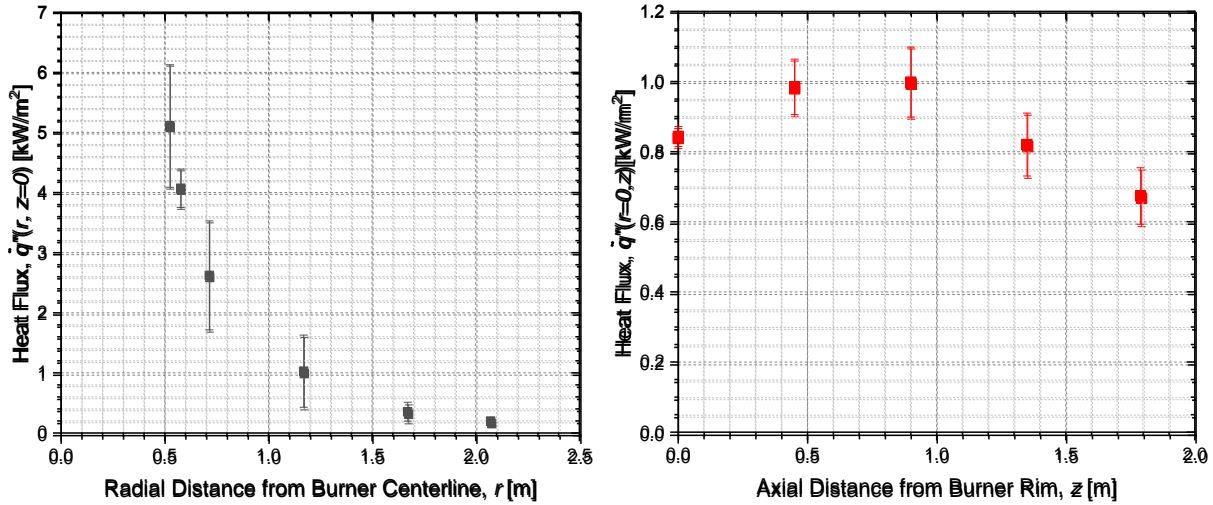


Figure 15. Mean and variance of heat flux as a function of; (a) radial distance from the burner centerline, (b) axial distance from the burner rim.

Figure 16 shows the mean and variance of heat flux distribution in the radial and axial directions, compared to 100 cm methanol pool fires in Ref. [11]. Radial heat flux values were in good agreement with the results of the previous study. As expected, the vertical heat fluxes were larger than those measured in Ref. [11] due to the position of the gauges, which were located at $r = 2.07$ m, rather than 3.3 m from the pool centerline. To compare the results in Figure 16 (b), heat flux values in Ref. [11] were scaled by the factor of $(3.3/2.07)^2$ based on the correlation of $q'' \sim 1/r^2$. The scaled heat fluxes agree with the results of the present study within experimental uncertainty as seen in Figure 16.

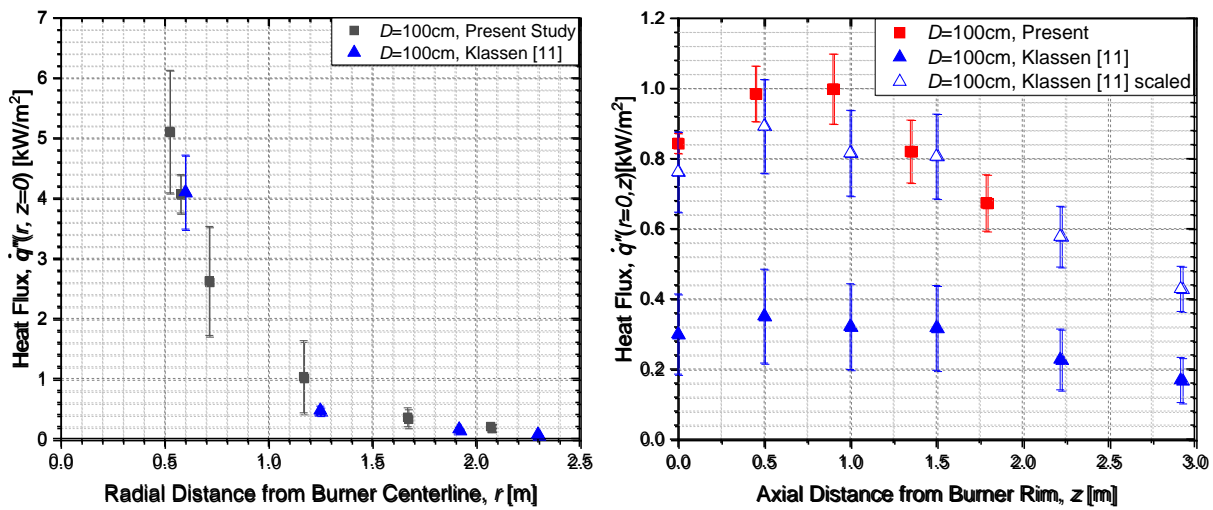


Figure 16. Mean and variance of heat flux as a function of; (a) radial distance from the burner centerline, (b) axial distance from the burner rim, compared to the results of 100 cm methanol pool fire in Ref. [11]; variance of all heat flux outputs in Ref. [11] was 15%.

Figure 17 (a) shows the mean and variance of the heat flux incident on the floor as a function of radial distance normalized by the pool diameter, comparing 7.1 cm, 30 cm and 100 cm methanol pool fires. The radial heat flux values were in good agreement with the results of the previous study. Figure 17 (b) shows the mean and variance of normalized heat flux as a function of axial distance normalized by the pool diameter.

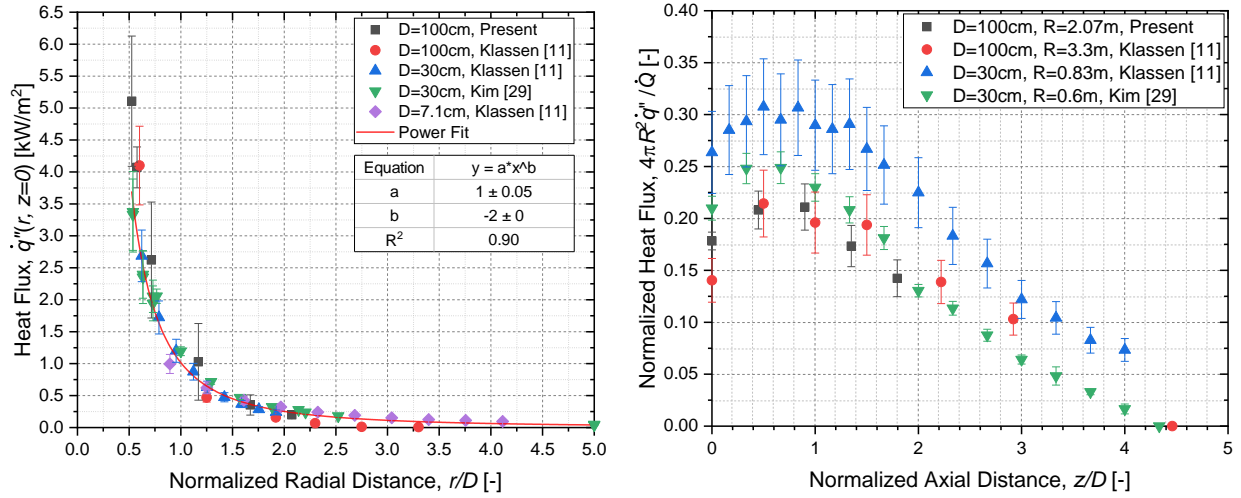


Figure 17. (a) mean and variance of heat flux as a function of radial distance normalized by the pool diameter, (b) mean and variance of normalized heat flux as a function of axial distance normalized by the pool diameter, compared to the results of 7.1 cm, 30 cm, and 100 cm methanol pool fire in Refs. [11, 29].

3.5.1. Radiative Fraction

The fraction of energy radiated from the fire, χ_{rad} , was calculated using Eqs. (8) and (9), considering the overall enthalpy balance explained in Ref. [29], where its value is equal to the ratio of the total radiative emission from the fire (\dot{Q}_{rad}) normalized by the idealized fire heat release rate (\dot{Q}). The radiative fraction (χ_{rad}) can be broken into the sum of the radiative heat transfer to the surroundings (χ_r) and onto the fuel surface (χ_{sr}) normalized by the heat release rate, such that:

$$\chi_{rad} = \chi_r + \chi_{sr} = \dot{Q}_{rad} / \dot{Q} \quad (8)$$

$$\chi_r = \dot{Q}_r / \dot{Q} \quad \text{and} \quad \chi_{sr} = \dot{Q}_{sr} / \dot{Q} \quad (9)$$

where \dot{Q}_r is the radiative energy emitted by the fire to the surroundings except to the fuel surface and \dot{Q}_{sr} is the radiative heat feedback to the fuel surface. Assuming symmetry, integrating the measured local radiative heat flux in the r and z directions (see Figure 3) yields the total energy radiated by the fire, \dot{Q}_{rad} , considering the flux through a cylindrical control surface about the pool fire:

$$\dot{Q}_{rad} = \dot{Q}_r + \dot{Q}_{sr} = \left(2\pi \int_{r_1}^{r_2} \dot{q}''(r, 0) \cdot r dr + 2\pi r_2 \int_0^{z_2} \dot{q}''(r_2, z) dz \right) + \pi r_1^2 \bar{\dot{q}}_{sr}'' \quad (10)$$

where r_1 and r_2 are 0.5 m and 2.07 m, z_2 is 3.62 m, and \bar{q}_{sr} is the average radiative heat flux incident on the fuel surface. In the energy balance for a steadily burning pool fire following Ref. [29], the total heat feedback (\dot{Q}_s) to the fuel surface is broken into radiative and convective components ($\dot{Q}_s = \dot{Q}_{sr} + \dot{Q}_{sc}$). Normalizing by \dot{Q} , then $\chi_s = \chi_{sr} + \chi_{sc}$. Kim, Lee and Hamins [29] measured the distribution of local heat flux incident on the fuel surface in a 30 cm methanol pool fire. The fractional total heat feedback (χ_s) was $0.082 \pm 24\%$ with 67% of the feedback attributed to radiation, that is, $\chi_{sr} = 0.055 \pm 21\%$. Here, the fractional heat feedback to the fuel surface (χ_s) in the 1 m pool fire is assumed to be about the same as in the 30 cm pool fire [29]. Using thin film theory, it is possible to estimate the convective heat transfer to the fuel surface following [30]:

$$\dot{Q}_{sc} = A \left(\frac{h}{C_p} \right) [\Delta H_c (\chi_a - \chi_{rad}) r_o / \chi_a - C_p (T_s - T_o)] y / (\exp(y) - 1) \quad (11)$$

where A is the pool surface area, $y (= \dot{m}'' C_p / h)$ is a blowing factor, \dot{m}'' is the fuel mass flux, r_o is the stoichiometric fuel/air mass ratio, T_s is the burner surface temperature, T_o is the ambient temperature, and C_p is the heat capacity of air taken here at 750 K, which is representative of a temperature intermediate between the flame temperature and the burner surface temperature. The heat transfer coefficient (h) is taken as $8.5 \text{ W}/(\text{m}^2 \text{ K})$ for a pool with “lips” [30]. Applying Eq. (11) yields $\chi_{sr} = 0.065 \pm 31\%$ and $\chi_{sr} / \chi_s = 0.80$, which is about 20% larger than its value in the 0.3 m methanol pool [29].

The fitting functions seen in Figure 18 and Figure 19 were used to integrate the heat flux in the radial and vertical directions. The zero-heat flux position ($z_2 = 3.62 \text{ m}$) was extrapolated from the values of the last two locations in Figure 19. In previous studies [11, 29], the heat flux peaked at a vertical position equal to approximately one half of the characteristic flame height and decreased almost linearly above the visible flame tip regardless of pool diameter and fuel type, until it reached zero. The vertical radiative heat flux (the second term in Eq. (10)) was integrated using the cubic function from 0 to z_1 (1.6 m) and either the cubic function or a line in the region from z_1 to z_2 . The energy difference associated with the fitting functions was treated as an uncertainty contribution to the measurement.

The values of the radiative heat loss and the radiative fraction are listed in Table A.5 of Appendix D.3. This value was applied to solve Eq. (10) for the 1 m methanol fire.

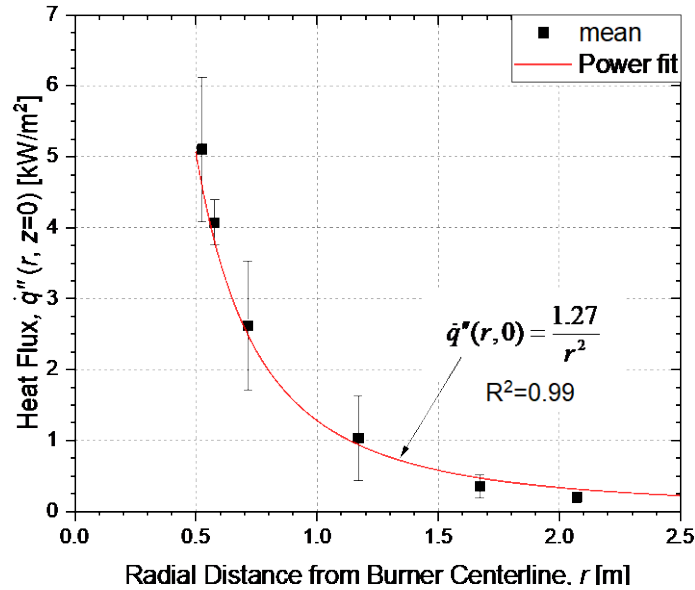


Figure 18. Mean and variance radial radiative heat flux in the downward direction as a function of radial distance from the burner centerline at the plane defined by the burner rim ($z=0$).

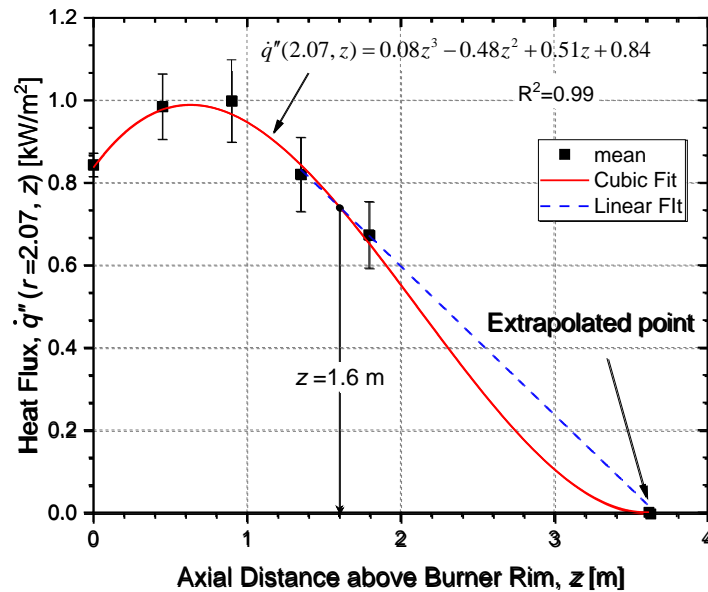


Figure 19. Mean and variance vertical radiative heat flux as a function of axial distance above the burner for gauges facing the pool fire and 2.07 m from the centerline.

The results showed that $\dot{Q}_{rad} = 56 \text{ kW} \pm 11 \%$ and $\chi_{rad} = 0.22 \pm 16 \%$. The radiative fraction of the total heat release rate emitted to the surroundings in previous studies for methanol pool fires is listed Table 2. The radiative fraction reported here for the 1 m methanol pool fire agrees with the value in Ref. [11] within expanded uncertainty (see Table 2). The radiative fraction for the 1 m pool fire was similar to its value in the 30 cm fire, and agreed with the result in Ref. [29] which showed that the radiative fraction was fairly constant for pool diameters less than 2 m.

Table 2. Comparison of the radiative fraction in steadily burning 30 cm and 100 cm methanol pool fires.

Research	Pool diameter	χ_{rad}
Present study	100 cm	$0.22 \pm 16\%$
Klassen and Gore [11]	100 cm	$0.19^{*\dagger}$
Kim, Lee and Hamins [29]	30 cm	$0.24 \pm 25\%$
Hamins, <i>et al.</i> [31]	30 cm	$0.22 \pm 10\%$
Klassen and Gore [11]	30 cm	$0.22^{*\dagger}$

* \bar{q}_s'' in Eq. (11) was assumed equal to the heat flux measured next to the burner ($\dot{q}''(r_1=R, 0)$), which yields $\chi_{sr} = 0.01$, which is smaller than expected [29]. χ_{rad} , therefore, was recalculated using $\chi_s = 0.082$ [28].

† Recalculated χ_{rad} , using $\Delta H_c = 19.918$ kJ/g [18], not 22.37 kJ/g assuming gaseous water as a product of combustion.

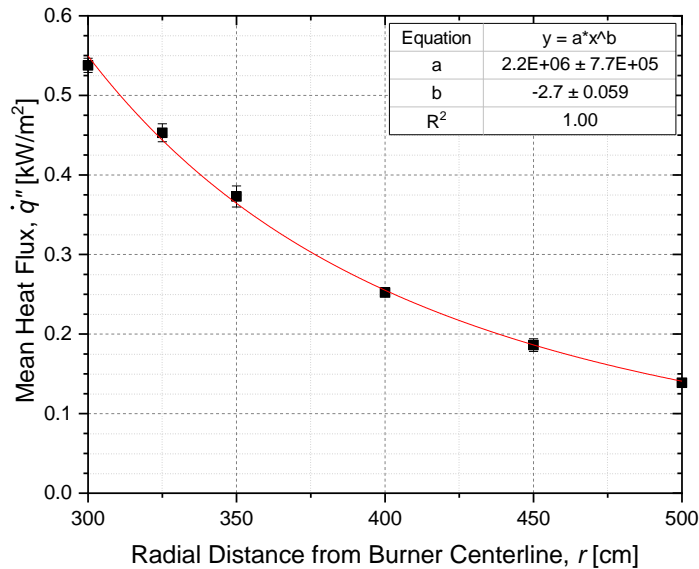


Figure 20. Mean and variance of heat flux as a function of radial distance from the burner centerline with the gauge directed towards the fire. The error bars indicate the variance of the mean heat flux for gauges located 40 cm, 60 cm and 80 cm above the burner.

Figure 20 shows the mean and variance of heat flux for Gauges 12 - 14 as a function of radial distance from the burner centerline. The radiative heat flux to an external element becomes more isotropic as the flame becomes optically thin or as the distance to the gauge increases [32]. Assuming isotropy, the radiative energy from the fire (\dot{Q}_{rad}) can be expressed as:

$$\dot{Q}_{rad} = 4\pi r^2 \dot{q}''(r, z) \quad (12)$$

Modak [32] suggests that a distance five times the diameter of the fire is adequate to use a single point location estimate of the total radiative flux. The results show the flame radiative power output under-

estimates the total radiative energy emitted by the flame with a bias of about 2 % at $r/D = 5$. Applying the single point estimate with the total radiative heat flux at $r = 500$ cm (i.e., $r/D = 5$), the estimated radiative fraction (χ_{rad}) is listed in Table 3; the uncertainty represents a 95 % confidence interval. The mean radiative fraction was 0.20 ± 34 %, which agrees with its value ($\chi_{rad} = 0.22$) calculated using Eq. (10).

Table 3. Radiative fraction based on the single point estimate method at $r = 500$ cm with combined expanded uncertainty, representing a 95 % confidence interval.

Axial distance above burner rim, z [cm]	Radiative fraction, χ_{rad} [-]
40	$0.19 \pm 33\%$
60	$0.20 \pm 37\%$
80	$0.19 \pm 33\%$

3.6. Liquid Fuel Temperature Profile

Figure 21 shows the mean fuel temperature and its variance as a function of the axial distance from the fuel surface in the pool fire test 1. The temperature of methanol increased from the bottom of the pool to the fuel surface until it approximately reached the boiling point of methanol at the pool surface. As expected, the liquid temperatures during Measurement 2 was higher than the temperatures during Measurement 1, which was 35 min later in the experiment, as the liquid fuel had received additional heat feedback from the fire. The time difference between both measurements was 35 minutes. The key finding is confirmation that the surface temperature is approximately the boiling point within experimental accuracy as described by Spalding [33]. Appendix G provides a table enumerating the mean and variance of the liquid fuel temperature measurements as a function of distance below the fuel surface.

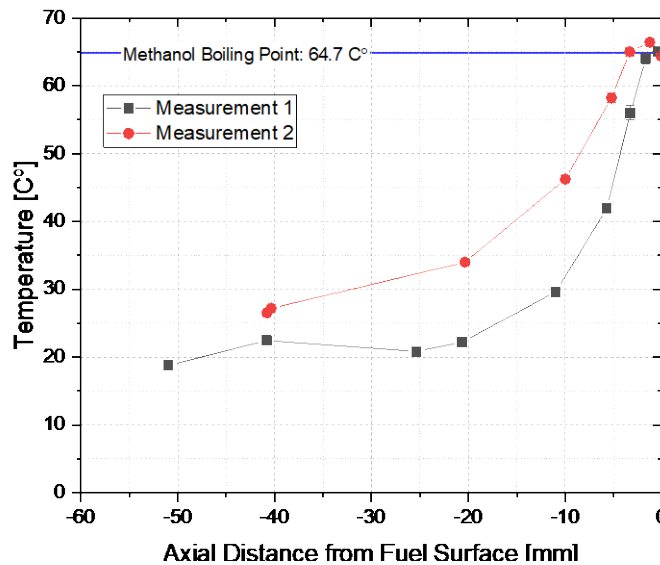


Figure 21. Mean and variance of fuel temperature as a function of the axial distance from the fuel surface in the pool fire test 1. The uncertainty in the temperature measurement is 2 °C [34].

4. Conclusions

A series of measurements were conducted to characterize the gas phase temperature, the burning rate, and heat release rate of a 1 m diameter, well-ventilated, methanol pool fire steadily burning in a quiescent environment. The gas-phase thermocouple temperatures were corrected considering radiative loss and thermal inertial effects. The corrected profile of mean axial temperature was shown to be similar to previous results for methanol pool fires when scaled by $\dot{Q}^{2/5}$.

The average steady-state mass burning rate was measured as $12.8 \text{ g/s} \pm 0.9 \text{ g/s}$, which yields an idealized heat release rate of $254 \text{ kW} \pm 19 \text{ kW}$. The measured heat release rate using oxygen consumption calorimetry was $256 \text{ kW} \pm 45 \text{ kW}$, which was consistent with the mass burning rate measurement. The maximum corrected mean and RMS temperature measured in the fire was $1371 \text{ K} \pm 247 \text{ K}$, which occurred on the centerline, 30 cm above the burner rim. The radiative fraction was $0.22 \pm 16 \%$, consistent with previous results. These results help characterize the structure of a 1 m diameter methanol pool fire and provide data that may be useful for the development and evaluation of fire models.

5. References

1. Akita, K. and Yumoto, T., Heat Transfer in Small Pools and Rates of Burning of Liquid Methanol, in *Proceedings of the Combustion Institute*, **10**, 943-948, (1965).
2. Hamins, A., Fischer, S. J., Kashiwagi, T., Klassen, M. E. and Gore, J. P., Heat Feedback to the Fuel Surface in Pool Fires, *Combustion Science and Technology*, **97**, 37-62, (1994).
3. Hostikka, S., McGrattan, K. B. and Hamins, A., Numerical Modeling of Pool Fires Using Les and Finite Volume Method for Radiation, *Fire Safety Science*, **7**, 383-394, (2003).
4. Weckman, E. J. and Strong, A. B., Experimental Investigation of the Turbulence Structure of Medium-Scale Methanol Pool Fires, *Combustion and Flame*, **105**, 245-266, (1996).
5. Yilmaz, A., *Radiation Transport Measurements in Methanol Pool Fires with Fourier Transform Infrared Spectroscopy*, NIST Grant/Contractor Report GCR 09-922, January 2009,
6. McGrattan, K., McDermott, R., Vanella, M., Hostikka, S., Floyd, J., Weinschenk, C. and Overholt, K., *Fire Dynamics Simulator User's Guide*, NIST Special Publication, 1019, National Institute of Standards and Technology, Gaithersburg, MD, October 2019, <http://dx.doi.org/10.6028/NIST.SP.1019>.
7. Maragkos, G., Beji, T. and Merci, B., Towards Predictive Simulations of Gaseous Pool Fires, *Proceedings of the Combustion Institute*, **37**, 3927-3934, (2019).
8. Chen, Z., Wen, J., Xu, B. and Dembele, S., Large Eddy Simulation of a Medium-Scale Methanol Pool Fire Using the Extended Eddy Dissipation Concept, *International Journal of Heat and Mass Transfer*, **70**, 389-408, (2014).
9. Tieszen, S. R., O'Hern, T. J., Schefer, R. W., Weckman, E. J. and Blanchat, T. K., Experimental Study of the Flow Field in and around a One Meter Diameter Methane Fire, *Combustion and Flame*, **129**, 378-391, (2002).
10. Tieszen, S. R., O'Hern, T. J., Weckman, E. J. and Schefer, R. W., Experimental Study of the Effect of Fuel Mass Flux on a 1-M-Diameter Methane Fire and Comparison with a Hydrogen Fire, *Combustion and Flame*, **139**, 126-141, (2004).
11. Klassen, M. and Gore, J., *Structure and Radiation Properties of Pool Fires*, NIST-GCR-94-651, National Institute of Standards and Technology, Gaithersburg, MD, June 1994,
12. Peacock, R. D., Jones, W., Reneke, P. and Forney, G., Cfast-Consolidated Model of Fire Growth and Smoke Transport (Version 6) User's Guide, *NIST Special Publication 1041r1*, National Institute of Standards and Technology, Gaithersburg, MD, 2013.
13. McGrattan, K., Hostikka, S., McDermott, R., Floyd, J., Weinschenk, C. and Overholt, K., *Fire Dynamics Simulator User's Guide*, National Institute of Standards and Technology, Gaithersburg, MD, 2016.
14. Bryant, R. A. and Bundy, M. F., *The NIST 20 MW Calorimetry Measurement System for Large-Fire Research*, NIST TN-2077, National Institute of Standards and Technology, Gaithersburg, MD, 2019, <https://doi.org/10.6028/NIST.TN.2077>.
15. Bergman, T. L., Incropera, F. P. and Lavine, A. S., *Fundamentals of Heat and Mass Transfer*, John Wiley & Sons, 2011.
16. Shaddix, C. R., *Correcting Thermocouple Measurements for Radiation Loss: A Critical Review*, American Society of Mechanical Engineers, New York, NY (US); Sandia National Labs., Livermore, CA (US), 1999.
17. Ranz, W. and Marshall, W. R., Evaporation from Drops, *Chem. Eng. Prog.*, **48**, 141-146, (1952).

18. Design Institute for Physical Properties (DIPPR 801), American Institute of Chemical Engineers, 2017.
19. Jaeger, F. M. and Rosenbohm, E., The Exact Formulae for the True and Mean Specific Heats of Platinum between 0° and 1600°C, *Physica*, **6**, 1123-1125, (1939).
20. Taylor, J., Introduction to Error Analysis, the Study of Uncertainties in Physical Measurements, 1997.
21. Otsu, N., A Threshold Selection Method from Gray-Level Histograms, *IEEE transactions on systems, man, and cybernetics*, **9**, 62-66, (1979).
22. Heskestad, G., Luminous Heights of Turbulent Diffusion Flames, *Fire Safety Journal*, **5**, 103-108, (1983).
23. Weckman, E. J. and Sobiesiak, A., The Oscillatory Behaviour of Medium-Scale Pool Fires, in *Proceedings of the Combustion Institute*, **22**, 1299-1310, (1989).
24. Baum, H. R. and McCaffrey, B. J., Fire Induced Flow Field-Theory and Experiment, in *Proceedings of the second international symposium on fire safety science*, Hemisphere, New York, **2**, 129-148, (1989).
25. Hamins, A., Yang, J. C. and Kashiwagi, T., An Experimental Investigation of the Pulsation Frequency of Flames, *Proceedings of the Combustion Institute*, **24**, 1695-1702, (1992).
26. Falkenstein-Smith, R., Hamins, A., Sung, K. and Chen, J. The Structure of Medium-Scale Pool Fire, in preparation, NIST Technical Note, National Institute of Standards and Technology, Gaithersburg, 2019.
27. Hamins, A. and Lock, A., *The Structure of a Moderate-Scale Methanol Pool Fire*, NIST Technical Note 1928, National Institute of Standards and Technology, Gaithersburg, MD, 2016,
28. Wang, Z., Tam, W. C., Lee, K. Y. and Hamins, A., *Temperature Field Measurements Using Thin Filament Pyrometry in a Medium-Scale Methanol Pool Fire*, NIST Technical Note 2031, National Institute of Standards and Technology, Gaithersburg, MD, 2018,
29. Kim, S. C., Lee, K. Y. and Hamins, A., Energy Balance in Medium-Scale Methanol, Ethanol, and Acetone Pool Fires, *Fire Safety Journal*, **107**, 44-53, (2019).
30. Orloff, L. and De Ris, J., Froude Modeling of Pool Fires, *Symposium (International) on Combustion*, **19**, 885-895, (1982).
31. Hamins, A., Klassen, M., Gore, J. and Kashiwagi, T., Estimate of Flame Radiance Via a Single Location Measurement in Liquid Pool Fires, *Combustion and Flame*, **86**, 223-228, (1991).
32. Modak, A. T., Thermal Radiation from Pool Fires, *Combustion and Flame*, **29**, 177-192, (1977).
33. Spalding, D. B., The Combustion of Liquid Fuels, *Proceedings of the Combustion Institute*, **4**, 847-864, (1953).
34. Omega Engineering Inc., *The Temperature Handbook*, Vol. MM, pages Z-39-40, Stamford, CT., 2004.
35. Taylor, B. N. and Kuyatt, C. E., *Guidelines for Evaluating and Expressing the Uncertainty of Nist Measurement Results*, NIST Technical Note 1297, National Institute of Standards and Technology, Gaithersburg, MD, 1994,
36. Holman, J. P., *Experimental Methods for Engineers*, McGraw-Hill, New York, 2001.
37. Kline, S., The Purposes of Uncertainty Analysis, *Journal of Fluids Engineering*, **107**, 153-160, (1985).
38. Bevington, P. R., Robinson, D. K., Blair, J. M., Mallinckrodt, A. J. and McKay, S., Data Reduction and Error Analysis for the Physical Sciences, *Computers in Physics*, **7**, 415-416, (1993).
39. Heskestad, G., Fire Plumes, Flame Height and Air Entrainment, Vol 1, Chap. 13, in (M. J. Hurley. Ed), *SFPE Handbook of Fire Protection Engineering*, 5th edition, Society of Fire Protection Engineers, Springer, New York, 2016.

40. Bryant, R., Johnsson, E., Ohlemiller, T. and Womeldorf, C., Estimates of the Uncertainty of Radiative Heat Flux Calculated from Total Heat Flux Measurements, in *Proc. 9th Interflam Conference in Edinburgh, Interscience Communications London*, 605-616, (2001).
41. Pitts, W. M., Lawson, J. R. and Shields, J. R., *NIST/BFRL Calibration System for Heat-Flux Gages*, Report of Test FR 4014, National Institute of Standards and Technology, Gaithersburg, MD, August 2001,
42. Bradley, D. and Matthews, K. J., Measurement of High Gas Temperatures with Fine Wire Thermocouples, *Journal of Mechanical Engineering Science*, **10**, 299-305, (1968).
43. Petit, C., Gajan, P., Lecordier, J. C. and Paranthoen, P., Frequency Response of Fine Wire Thermocouple, *Journal of Physics E: Scientific Instruments*, **15**, 760-770, (1982).
44. Slack, G. A., Platinum as a Thermal Conductivity Standard, *Journal of Applied Physics*, **35**, 339-344, (1964).

Appendices

A. Thermal Properties

A.1. Thermochemical properties of methanol at =20 °C [18]

Fuel	Chemical Formula	$\rho(T=20\text{ °C})$ [kg/m ³]	MW [g/mol]	T_b [°C]	ΔH_C ($T=20\text{ °C}$) [kJ/g]	ΔH_L^* ($T=20\text{ °C}$) [kJ/g]
Methanol	CH ₃ OH	794 ± <1%	32.04	64.70 ± <1%	19.9 ± <1%	1.18 ± <3%
* $\Delta H_L(T=T_b) = 1.10\text{ kJ/g} \pm <3\%$						

A.2. Thermophysical properties of a platinum thermocouple [16, 19]

Temperature [K]	Specific heat [J/g-K]*	Emissivity†
373	0.13523	0.00459
473	0.13775	0.02759
573	0.14026	0.04871
673	0.14319	0.06808
773	0.1457	0.08583
873	0.14821	0.10209
973	0.15072	0.11699
1073	0.15324	0.13067
1173	0.15575	0.14325
1273	0.15826	0.15486
1373	0.16077	0.16564
1473	0.16329	0.17571
1573	0.1658	0.18521
1673	0.16831	0.19427

*from Ref. [19]

†from Ref. [16]

A.2.1. Curve fitting functions of thermophysical properties of thermocouple

$$\begin{aligned}
 c_{p,b} &= 0.13 + 2.56T \\
 \varepsilon_b &= -0.1 + 3.24E-4T - 1.25E-7T^2 + 2.18E-11T^3
 \end{aligned}
 \tag{A.1}$$

A.3. Thermophysical properties of air [18]

Temperature [°C]	Density ρ [kg/m ³]	Specific Heat c_p [J/kg-K]	Thermal Conductivity λ [W/m-K]	Dynamic Viscosity μ [kg/m-s]	Prandtl Number Pr [-]
300	0.6158	1044	0.04418	2.93E-05	0.6935
350	0.5664	1056	0.04721	3.10E-05	0.6937
400	0.5243	1069	0.05015	3.26E-05	0.6948
450	0.488	1081	0.05298	3.42E-05	0.6965
500	0.4565	1093	0.05572	3.56E-05	0.6986
600	0.4042	1115	0.06093	3.85E-05	0.7037
700	0.3627	1135	0.06581	4.11E-05	0.7092
800	0.3289	1153	0.07037	4.36E-05	0.7149
900	0.3008	1169	0.07465	4.60E-05	0.7206
1000	0.2772	1184	0.07868	4.83E-05	0.726
1500	0.199	1234	0.09599	5.82E-05	0.7478
2000	0.1553	1264	0.11113	6.63E-05	0.7539

A.3.1. Curve fitting functions of thermophysical properties of air

$$\begin{aligned}
 \rho_{air} &= 351.90(T + 272.99)^{-0.9996} \\
 c_{p,air} &= 948.38 + 0.36 \cdot T - 1.43E-4 \cdot T^2 + 2.20E-8 \cdot T^3 \\
 \lambda_{air} &= 0.024 + 7.56E-5 \cdot T - 2.52E-8 \cdot T^2 + 4.64E-12 \cdot T^3 \\
 \mu_{air} &= 1.74E-5 + 4.63E-8 \cdot T - 2.40E-11 \cdot T^2 + 1.05E-14 \cdot T^3 - 1.99E-18 \cdot T^4
 \end{aligned}
 \tag{A.2}$$

B. Bead temperature and gas temperature

Table A.1. Mean and variance of measured bead temperature and corrected gas temperature as a function of the axial and radial distance from the burner centerline; the combined uncertainty is a 95 % confidence interval.

Z [cm]	R [cm]	Mean Bead Temperature T_b [K]	SD [K]	Mean Gas Temperature T_g [K]	SD [K]	U_c [%]	Z [cm]	R [cm]	Mean Bead Temperature T_b [K]	SD [K]	Mean Gas Temperature T_g [K]	SD [K]	U_c [%]
5	0	1129	252	1141	296	52	100	30	522	198	523	227	87
10	0	1253	244	1272	288	48	100	40	441	151	441	173	78
20	-10	1291	237	1311	280	43	100	50	380	102	380	115	61
20	0	1335	211	1357	250	37	110	0	748	239	751	277	74
20	10	1297	232	1317	273	42	120	0	693	217	695	252	73
20	20	901	322	908	372	82	130	0	630	191	631	220	70
20	30	674	327	677	375	111	140	-10	552	169	553	196	71
20	40	465	271	467	306	131	140	0	620	185	621	214	69
20	50	302	48	303	55	36	140	10	622	197	623	226	73
30	0	1347	209	1371	247	36	140	20	549	177	549	206	75
40	0	1330	225	1352	264	39	140	30	488	149	488	171	70
60	-10	1016	301	1025	346	68	140	40	428	122	428	141	66
60	0	1217	263	1234	309	50	140	50	391	95	391	110	56
60	10	1105	294	1118	343	61	160	0	561	155	561	179	64
60	20	733	293	736	339	92	180	-10	516	128	516	149	58
60	30	541	245	542	280	103	180	0	515	121	515	140	54
60	40	443	197	444	222	100	180	10	514	134	515	154	60
60	50	338	102	338	112	66	180	20	462	111	462	129	56
80	0	1000	286	1009	333	66	180	30	413	96	413	111	54
100	-10	701	247	703	284	81	180	40	393	91	393	105	54
100	0	816	267	820	310	76	180	50	351	68	351	78	45
100	10	816	275	820	319	78	200	0	472	96	472	111	47
100	20	696	261	698	304	87	210	0	458	92	458	106	46

C. Heat flux gauge information

Table A.2. Heat flux gauge locations from the burner centerline and calibration factor.

Index	S/N	Full scale [kW/m ²]	Position (R, Z) [cm]	Responsivity [(kW/m ²)/mV]
1	183882	10	(207.5, 0)	0.98x
2	183881	10	(207.5, 45)	0.96x
3	62772	50	(207.5, 90)	6.57x -0.1
4	74991	20	(207.5, 135)	1.47x -0.12
5	183892	10	(207.5, 179.5)	1.38x +0.0086*
6	146132	200	(52.5, 0)	16.56x +0.043
7	177176	200	(57.7, 0)	17.74x +0.084
8	177175	200	(71.5, 0)	17.92x +0.21
9	5256	100	(117, 0)	10.94x -0.090
10	150823	20	(167.2, 0)	2.28x -0.081
11	183891	10	(207.2, 0)	0.93x
12	208971	1	(300-500, 40)	0.13x
13	198292	2	(300-500, 60)	0.18x
14	198291	5	(300-500, 80)	0.69x
*with ZnSe window (204993)				

D. Heat flux

D.1. Radial heat flux

Table A.3. Mean and variance of radial heat flux as a function of the radial distance from the burner centerline.

Z [cm]	R [cm]	\dot{q}'' [kW/m ²]	SD [kW/m ²]	$U_c(\dot{q}'')$ [%]
0	52.5	5.1	1.0	40
0	57.7	4.1	0.3	16
0	71.5	2.6	0.9	69
0	117	1.0	0.4	117
0	167.2	0.4	0.2	90
0	207.2	0.2	0.1	52

D.2. Vertical heat flux

Table A.4. Mean and variance of vertical heat flux as a function of the axial distance from the burner rim.

Z [cm]	R [cm]	\dot{q}'' [kW/m ²]	SD [kW/m ²]	$U_c(\dot{q}'')$ [%]	Z [cm]	R [cm]	\dot{q}'' [kW/m ²]	SD [kW/m ²]	$U_c(\dot{q}'')$ [%]
0	207.5	0.84	0.03	8	60	450	0.22	0.03	24
40	300	0.56	0.03	13	60	500	0.16	0.03	36
40	325	0.47	0.03	15	80	300	0.56	0.03	13
40	350	0.39	0.04	19	80	325	0.47	0.03	15
40	400	0.27	0.03	22	80	350	0.39	0.04	19
40	450	0.20	0.02	23	80	400	0.27	0.03	22
40	500	0.16	0.03	32	80	450	0.20	0.02	23
45	207.5	0.98	0.08	17	80	500	0.16	0.03	32
60	300	0.57	0.03	12	90	207.5	1.00	0.10	21
60	325	0.49	0.03	14	135	207.5	0.82	0.09	22
60	350	0.41	0.03	17	179.5	207.5	0.67	0.08	24
60	400	0.28	0.03	22					

D.3. Radiative heat and Radiative fraction

Table A.5. Radiative heat emitted from the fire and radiative fraction calculated by the integration method.

Radiative heat		Radiative fraction	
\dot{Q}_r	39 kW ± 6%	χ_r	0.15 ± 18%
\dot{Q}_{sr}	17 kW ± 36%	χ_{sr}	0.065 ± 31%
\dot{Q}_{rad}	56 kW ± 11%	χ_{rad}	0.22 ± 16%

E. Background Heat Flux Estimate

The measured heat flux can be affected by the temperature of surroundings (walls, floor) and changes in cooling water temperature of gauges during the experiment. The ambient air temperature and the cooling water temperature were maintained on consistently $26\text{ }^{\circ}\text{C} \pm 0.8\text{ }^{\circ}\text{C}$ and $15\text{ }^{\circ}\text{C} \pm 0.1\text{ }^{\circ}\text{C}$, averaged from 2000 s to 5000 s as seen in Figure A.1.

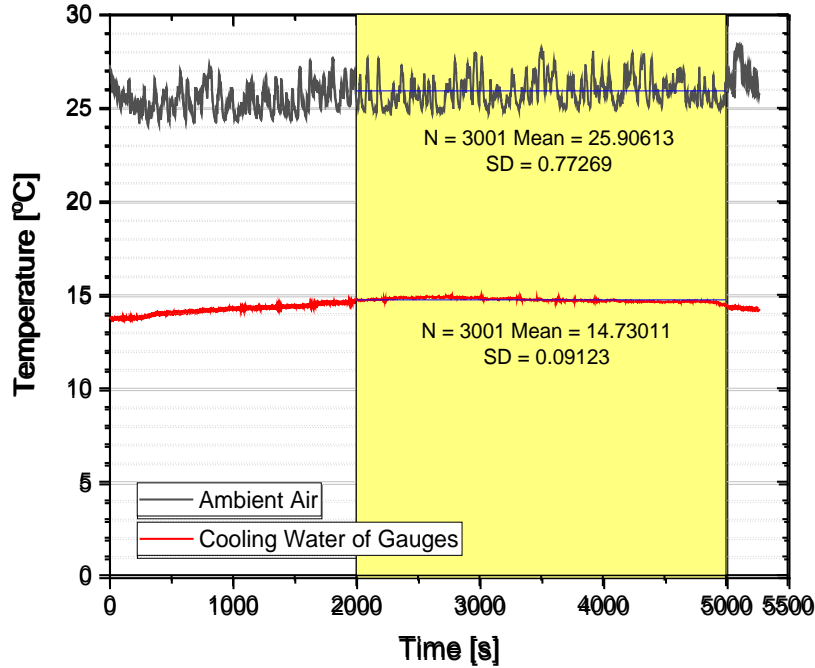


Figure A.1. Ambient temperature and cooling water temperature of gauges as a function of time during the experiment of Test 1. The yellow region indicates the average window.

Figure A.2 shows the background heat flux estimation for gauge 12 seen in Figure 3 of Section 2.3. The initial background value (\dot{q}_i'') was 0.11 kW/m^2 which is the averaged value 50 s before ignition (time (t_i) = 250 s). The post background value (\dot{q}_p'') was about 0.21 kW/m^2 which was estimated considering the sudden change in the slope of the signal at the fire extinguishing time (t_p) of 4850 s. Initial and post backgrounds heat fluxes for all gauges are listed in Table A.6.

Table A.6. Initial and post background fluxes

Gauge no.	Z [cm]	\dot{q}_i''	\dot{q}_p''
12	40	0.11	0.20
13	60	0.11	0.21
14	80	0.11	0.20

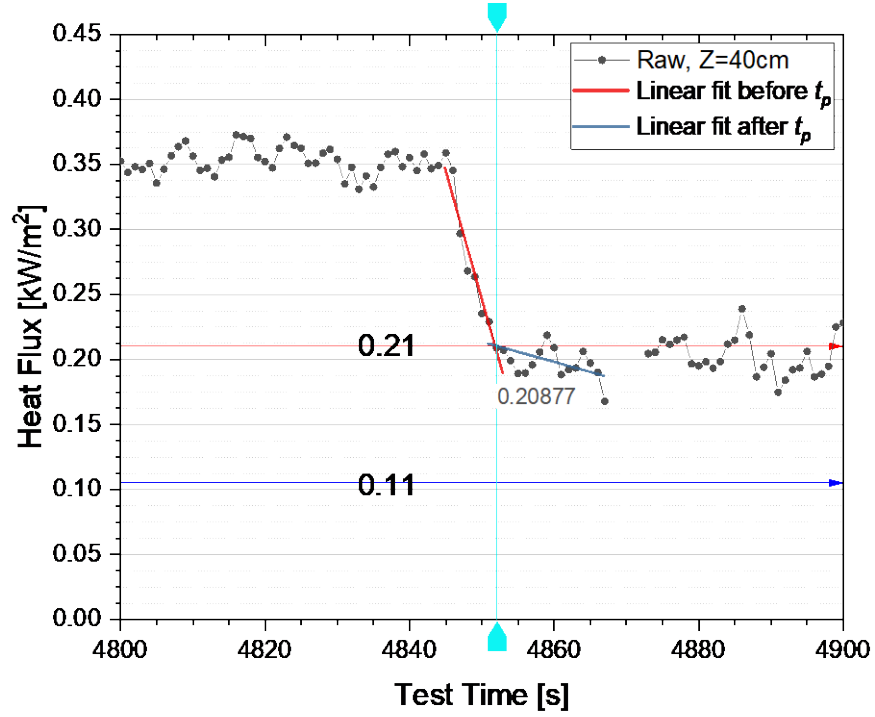


Figure A.2. Post background heat flux estimation for the gauge 12.

To estimate the background heat flux changes during the experiment, the time-averaged heat fluxes were compared. Figure A.3 shows the uncorrected(raw) heat flux as a function of time and comparison of heat flux at $r=500\text{cm}$ for gauges 12 – 14. The heat flux measured at the same position increased 0.02 kW/m^2 during the steadily burning. So, the background heat flux (\dot{q}_b'') change was estimated assuming the background heat flux increased linearly with time:

$$\dot{q}_b'' = (\dot{q}_p'' - 0.02) + \frac{0.02}{t_e - t_s} (t - t_s) \quad (\text{A.3})$$

where t is the instantaneous time, t_s is the start of steady burning (850 s) and t_e is the end time (4815 s).

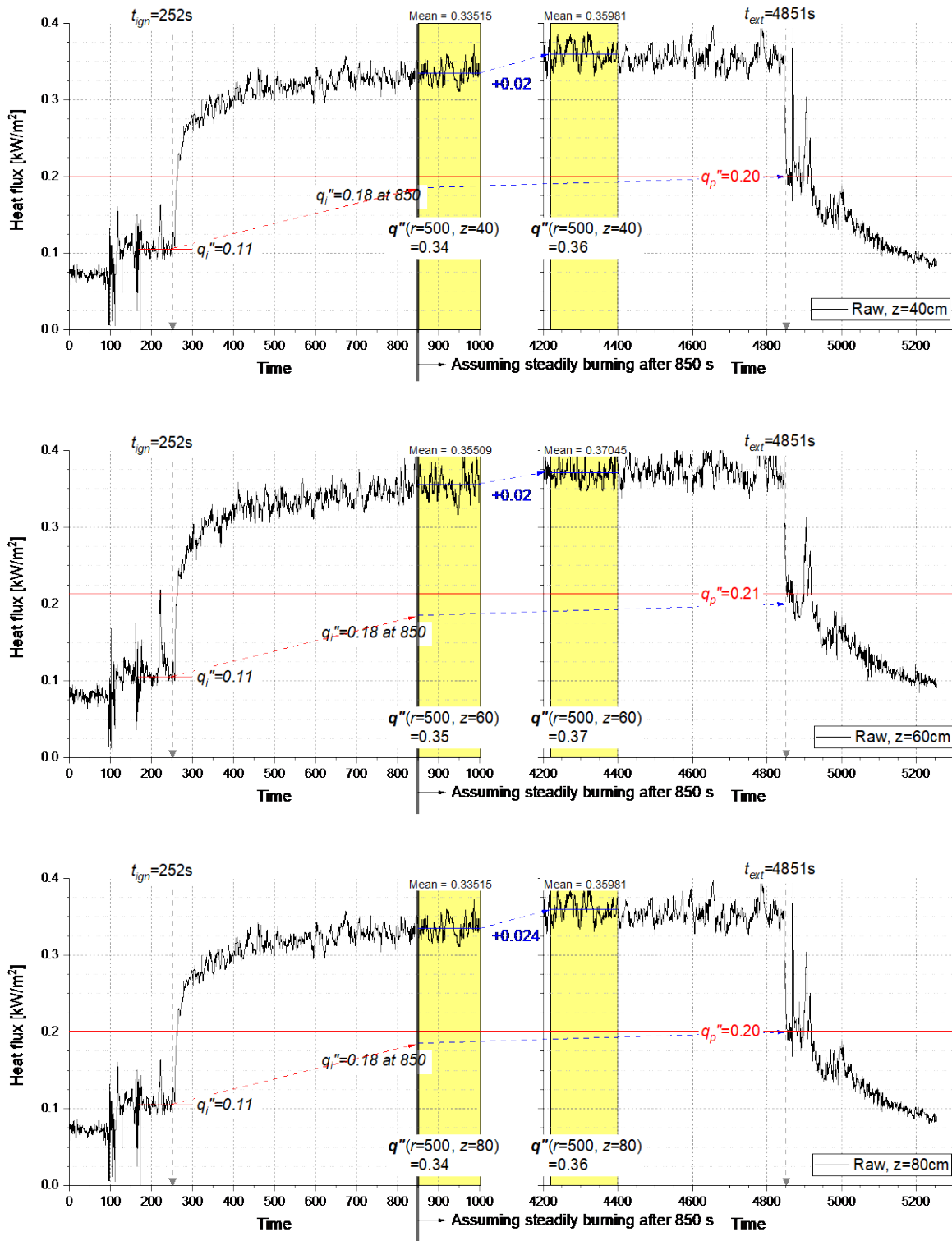


Figure A.3. Uncorrected heat flux as a function of time and comparison of mean heat flux at $r=500$ cm in each gauge

F. Uncertainty Analysis

Here, we discuss the uncertainty analysis for the temperature, heat flux and radiative fraction determinations. The uncertainty analysis follows Taylor and Kuyatt [35]. A series of measurements, y , can be expressed as a function of its associated independent variables, some of which are direct measurements. The function f in Eq. (A.4) contains all quantities that significantly contribute to the measurement:

$$y = f(x_1, x_2, x_3, \dots, x_n) \quad (\text{A.4})$$

If the uncertainties of independent variables (x_i) are uncorrelated, the combined relative uncertainty ($u_c(y)/y$) of the result, y , is given by Eq. (A.5). [20, 36, 37]

$$\frac{u_c(y)}{y} = \sum_{i=1}^n \sqrt{s_i \frac{u(x_i)}{x_i}} \quad (\text{A.5})$$

where $u_c(x_i)$ is the combined standard uncertainty and $u(x_i)$ is the standard uncertainty of each variable (x_i). s_i is the non-dimensional sensitivity coefficient, defined as Eq. (A.6)., determining the contribution of uncertainty for its variable to the combined uncertainty.

$$s_i = \frac{\partial f}{\partial x_i} \frac{x_i}{y} \quad (\text{A.6})$$

Combined expanded uncertainty (U_c) is defined as:

$$U_c = k u_c(y) \quad (\text{A.7})$$

where k is a coverage factor. Typically, k is in the range 2 to 3 and $U_c = 2u_c(y)$ defines an interval having a level of confidence of approximately 95 %.

F.1. Gas Temperature

The measured temperature (T_b) was corrected considering an energy balance at the thermocouple bead:

$$T_g = T_b + \frac{\rho_b c_{p,b} d_b^2}{6\lambda_g \text{Nu}} \frac{dT_b}{dt} + \frac{\epsilon_b \sigma d_b (T_b^4 - T_{surr}^4)}{\lambda_g \text{Nu}} \quad (\text{A.8})$$

On the right side of Eq. (A.8), the first term is the bead temperature (T_b) and the last two terms represent thermal inertial correction temperature (T_{the}) and radiation correction temperature (T_{rad}) terms, respectively. The uncertainty of each term was estimated and then combined to calculate the uncertainty of the gas temperature (T_g) using the weighted-sum method [38]. The variance (σ) of the gas temperature (T_g) is calculated considering the variance of the three terms in Eq. A8 multiplied by their weight factors.

$$\sigma(T_g)^2 = a^2 \sigma(T_b)^2 + b^2 \sigma(T_{the})^2 + c^2 \sigma(T_{rad})^2 \quad (\text{A.9})$$

where, weight factors are defined as $a = \mu(T_b) / \mu(T_g)$, $b = \mu(T_{the}) / \mu(T_g)$, $c = \mu(T_{rad}) / \mu(T_g)$. Then, the combined relative uncertainty of gas temperature is estimated as:

$$u_c(T_g) = \frac{\sigma(T_g)}{\mu(T_g)} \quad (\text{A.10})$$

where $\mu(T_g)$ is the mean gas temperature corrected for thermal inertial and radiative exchange effects.

F.1.1. Bead Temperature Uncertainty

The variance of the measured bead temperature and calibration error of the thermocouple contribute to the combined uncertainty of the bead temperature, $u_c(T_b)$ as below:

$$u_c(T_b)^2 = u(T_b)^2 + u(T_{cal})^2 \quad (\text{A.11})$$

where $u(T_{cal})$ is 0.25% according to the manufacturer [34]. The variance of the measured temperature represents the uncertainty of the bead temperature. Typically, $u(T_{cal})$ is much smaller (5%) than $u(T_b)$.

F.1.2. Uncertainty of the Thermal Inertia Correction

The thermal inertia correction term can be expressed as a function of thermophysical properties of the thermocouple bead, the bead diameter and the Nusselt number.

$$T_{the} = \frac{\rho_b c_{pb} d_b^2}{6\text{Nu}} \frac{dT_b}{dt} \quad (\text{A.12})$$

Propagating the error, $u_c(T_{the})$ can be expressed as:

$$u_c(T_{the}) = u(\rho_b)^2 + u(c_{pb})^2 + 4u(d_b)^2 + u(\text{Nu})^2 + u(dT_b/dt)^2 \quad (\text{A.13})$$

Uncertainty in the density (ρ_b) and specific heat (c_{pb}) of the thermocouple bead were calculated using the fitting function in the appendix. Uncertainties of the bead diameter and the Nusselt number are described below.

F.1.2.1. Uncertainty of Bead Diameter

The bead diameter was measured using Image-J image processing software from a photo taken with a microscope. The uncertainty of the bead diameter was multiplied by the image resolution and the number of pixels needed to determine the edge of bead. The image resolution was 1.6 μm per pixel. At least 3 pixels were needed to determine the boundary of the bead. The measured bead diameter was $153.3 \mu\text{m} \pm 10 \mu\text{m}$ in Figure 2.

F.1.2.2. Uncertainty of Nusselt Number

The choice of Nusselt number is conventionally based on the geometry of the bead being spherical or cylindrical. Bead shape was taken as spherical based on its microscope photo image. The most commonly used Nusselt number models for low-Re forced convection over a sphere are those given by Ranz and Marshall [17]. The Nusselt number (Nu) is a function of Reynolds number (Re) and Prandtl number (Pr).

$$\text{Nu} = 2.0 + 0.6\text{Re}_d^{1/2}\text{Pr}^{1/3}; \quad 0 < \text{Re} < 200 \quad (\text{A.14})$$

Mean plume velocity and the maximum velocity were estimated as 5.5 m/s and 6.0 m/s, respectively, using a point source buoyancy-plume theory [39] (see the appendix I). The range of Re was calculated as velocity (U_g) and bead diameter (d_b) are 6 m/s and 150 μm , respectively. Fig. 2 shows the Reynolds number as a function of temperature. As a result, the maximum Re is about 17, which satisfies the limit of the Ranz-Mashall model.

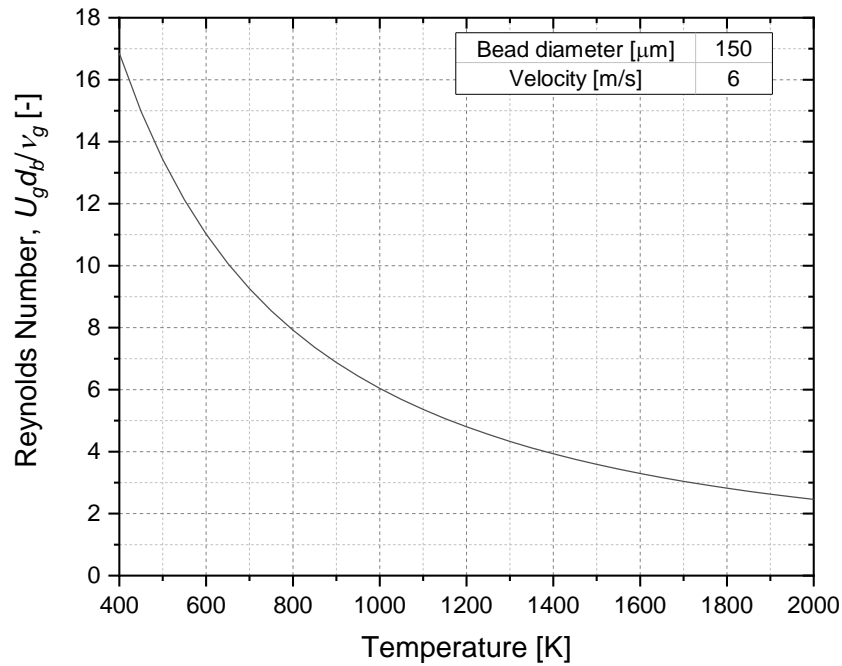


Figure A.4 Reynolds number as a function of temperature in $U_g = 6$ m/s and $d_b = 150$ μm .

Based on Eq. (A.14), the combined uncertainty in Nu can be expressed:

$$u_c(\text{Nu})^2 = \frac{1}{4}u(\text{Re})^2 + \frac{1}{9}u(\text{Pr})^2 \quad (\text{A.15})$$

where ρ_g , μ_g , λ_g and c_{pg} associated with Re or Pr are dependent on the gas temperature. Those values were calculated using fitting functions as seen in the appendix A.

F.1.3. Uncertainty of Radiation Correction

Radiation correction temperature (T_{rad}) in Eq. (A.8) can be simplified with $T_b^4 \gg T_{surr}^4$:

$$T_{rad} \cong \frac{\epsilon_b \sigma d_b T_b^4}{\lambda_g \text{Nu}} \quad (\text{A.16})$$

where σ is the Stefan-Boltzmann constant ($5.67 \cdot 10^{-8} \text{ W/m}^2 \text{ K}^4$) and ϵ_b is the emissivity of platinum, which is a function of temperature. Propagation of error leads to:

$$u_c(T_{rad})^2 = u(\epsilon_b)^2 + u(\lambda_g)^2 + u(d_b)^2 + u(\text{Nu})^2 + 4^2 u(T_b)^2 \quad (\text{A.17})$$

F.2. Heat Flux

Heat flux gauges were calibrated using a secondary standard gauge in a well-characterized calibration facility. The calibration method and apparatus are described in Ref. [40]; the systematic uncertainty for the calibration ($u(\text{cal.})$) was estimated as 2.3 % [41] and the combined expanded uncertainty of the measured heat flux was estimated as:

$$U_c(\dot{q}'') = 2\sqrt{u(\dot{q}'') + u(\text{cal.})} \quad (\text{A.18})$$

F.3. Radiative Fraction

F.3.1. Radiative Fraction Based on Fitting Functions

To calculate the vertical radiative heat flux, the second term in Eq. (10) was integrated using the cubic function either the cubic or a linear function depending on the integration region. The energy difference due to fitting functions was treated as uncertainty, i.e., $u(\dot{Q}_{r,fit})$.

$$U_c(\chi_{rad}) = 2\sqrt{u(\dot{Q}_{r,fit})^2 + u(\dot{Q}_{sr})^2 + u(\dot{Q})^2} \quad (\text{A.19})$$

where $u(\dot{Q}_{sr})$ is the combined uncertainty of fractional radiative heat feedback on the fuel surface which is 10.5 % in Ref. [29]. $u(\dot{Q})$ is the combined uncertainty of heat release rate measured from the calorimetry which is 3.4 % in Ref. [14]. $\dot{Q}_{r,fit}$ was $39 \text{ kW} \pm 2.94\%$.

F.3.2. Radiative Fraction Based on a Single Point Estimate

Radiative fraction (χ_{rad}) is defined as \dot{Q}_{rad}/\dot{Q} . Modak [32] suggests that a distance five times the diameter of the fire is adequate to use a single point location estimate of the total radiative flux, assuming isotropy. For isotropic radiation, the radiative energy from the fire (\dot{Q}_{rad}) can be expressed as:

$$\dot{Q}_{rad} = 4\pi r^2 \dot{q}''(r, z) \quad (\text{A.20})$$

The results showed the flame radiative power output assuming radiative isotropy tends to underestimate the total radiative energy emitted by the flame with a bias of about 2 % at $r/D=5$. Here, it is a contribution to the uncertainty as $u(\dot{Q}_{rad,m})$. In Eq. (1), \dot{q}'' is the corrected heat flux subtracted the

background heat flux (\dot{q}_b'') from the measured heat flux (\dot{q}_m''), i.e., $\dot{q}'' = \dot{q}_m'' - \dot{q}_b''$. So, propagation of error for the heat flux can be expressed as:

$$u_c(\dot{q}'')^2 = \left(\frac{\sqrt{a^2\sigma(\dot{q}_b'')^2 + b^2\sigma(\dot{q}_m'')^2}}{\mu(\dot{q}'')} \right)^2 + u(\dot{q}_{cal}'')^2 \quad (\text{A.21})$$

where $u(\dot{q}_{cal}'')$ is the systematic uncertainty for the calibration, which estimated at 2.3 % [41]. Weight factors are defined as $a = \mu(\dot{q}_b'')/\mu(\dot{q}'')$ and $b = \mu(\dot{q}_m'')/\mu(\dot{q}'')$.

Finally, propagation of error for the radiative fraction leads to:

$$u_c(\chi_{rad})^2 = u(\dot{q}'')^2 + u(\dot{Q})^2 + u(\dot{Q}_{rad,m})^2 \quad (\text{A.22})$$

where $u(\dot{Q})$ is the uncertainty of the heat release rate using the burning rate measured by a scale.

G. Liquid Fuel Temperature

Table A.7. Mean and variance of liquid fuel temperature as a function of the axial distance underneath the fuel surface. The radial position of the thermocouple is 35 cm from the burner centerline. U is the expanded uncertainty, representing a 95 % confidence interval.

	Z [mm]	Temperature [°C]	SD [°C]	U [%]
Test 1	0.4	65	1	1.7
	-0.4	65	1	1.9
	-1.7	64	1	2.3
	-3.3	56	1	3.8
	-5.7	42	0	2.3
	-11.0	30	0	2.4
	-20.6	22	0	1.0
	-25.4	21	0	1.0
	-40.8	22	0	1.3
	-51.0	19	0	0.7
Test 2	-0.1	64	0	1.2
	-1.2	66	0	1.3
	-3.3	65	1	2.0
	-5.2	58	1	2.3
	-10.0	46	0	1.4
	-20.3	34	0	0.6
	-40.4	27	0	0.5
	-40.8	26	0	0.3

H. Cold Length of Thermocouple Wire

Thermal conduction along thermocouple wires can result in significant heat loss from the thermocouple wire and junction to the larger, cooler lead wires (cooler on account of increased radiation loss and conductive losses through the thermocouple support structure) [16]. Bradley and Matthews [42] showed that the conduction heat loss from the thermocouple wire and junction to the cooler prone can be significant if the length to diameter ratio, l/d_w , of the wire is lower than 200. Petit, *et al.* [43] suggested a better criterion based on the cold length (l_c) which is the characteristic length defined as:

$$l_c = \frac{d_w}{2} \sqrt{\frac{\lambda_w}{\lambda_g \cdot Nu}} \quad (\text{A.23})$$

where d_w and λ_w are the diameter and thermal conductivity of the wire, respectively. Assuming the wire is cylindrical, the Nusselt number correlation for the circular cylinder in crossflow [15] is as below:

$$Nu = 0.989 Re_d^{0.330} Pr^{1/3}; \quad 0.4 \leq Re_d \leq 4, \quad Pr \geq 0.7 \quad (\text{A.24})$$

According to Ref. [43], conductive heat loss is negligible if $l/l_c > 10$, this criterion accounts for both the characteristics of the flow and the thermocouple properties. Applying Eq. (A.24) to Eq. (A.23), the mean and RMS cold length averaged in $T_g = 400$ K to $T_g = 1600$ K was $0.94 \text{ mm} \pm 0.02 \text{ mm}$. The cold length and its variables depending on temperature are listed in Table A.8. Here, the distance between the bead and ceramic tube was 1 cm; thus, conductive heat loss was neglected for the bead in Section 2.2.

Table A.8. Cold length and its variables as a function of temperature in $U_g = 2 \text{ m/s}$, $d_w = 50 \text{ }\mu\text{m}$. The mean and variance of cold length is $0.94 \text{ mm} \pm 0.02\text{mm}$.

T_g [K]	v_g [m ² /s]	Re_d [-]	Pr [-]	Nu [-]	λ_w^* [W/m-K]	λ_g [W/m-K]	l_c [mm]
400	2.59E-05	3.9	0.69	1.36	71.5	3.37E-02	0.99
500	3.78E-05	2.6	0.68	1.20	72.0	4.04E-02	0.96
600	5.13E-05	2.0	0.68	1.08	72.6	4.66E-02	0.95
700	6.61E-05	1.5	0.68	1.00	73.4	5.24E-02	0.94
800	8.21E-05	1.2	0.69	0.93	74.5	5.77E-02	0.93
900	9.94E-05	1.0	0.70	0.88	75.7	6.28E-02	0.93
1000	1.18E-04	0.9	0.70	0.83	77.1	6.75E-02	0.93
1100	1.37E-04	0.7	0.71	0.79	78.7	7.21E-02	0.93
1200	1.57E-04	0.6	0.71	0.76	80.6	7.64E-02	0.93
1300	1.79E-04	0.6	0.72	0.73	82.6	8.05E-02	0.94
1400	2.01E-04	0.5	0.72	0.70	84.8	8.45E-02	0.94
1600	2.47E-04	0.4	0.72	0.66	89.9	9.20E-02	0.96

*from Ref. [44]

I. Plume Velocity Effect on Temperature Correction

Assuming the variations of density in the field of motion are small compared to the ambient density and the profiles of vertical velocity and buoyance force in horizontal sections are of similar form in all heights, mean plume velocity (\bar{u}_0) is estimated using considering a point source buoyancy-plume theory [39], which is defined as:

$$\bar{u}_0 = 3.4 \left(\frac{g}{c_{p,g} \rho_\infty T_\infty} \right)^{1/3} \dot{Q}_c^{1/3} (z - z_0)^{-1/3} \quad (\text{A.25})$$

where the factor of $3.4[g/(c_{p,g} \rho_\infty T_\infty)]^{1/3}$ has the numerical value of $1.03 \text{ m}^{4/3}/\text{s}/\text{kW}^{-1/3}$ in 1 atm, 300 K. \dot{Q}_c is the convective heat release rate. z is the elevation above the burner rim and z_0 is the virtual origin defined as $z_0 = -1.02D + 0.083\dot{Q}^{2/5}$. The details of the theory and assumptions are described in Ref. [39]. To calculate the mean plume velocity, the ratio of \dot{Q}_c/\dot{Q} was taken as 0.8 based on $\chi_{rad} = 0.2$ from Table 3. and z_0 was -0.26 m using $\dot{Q} = 256 \text{ kW}$. The measured plume height of $1.1 \text{ m} \pm 20\%$ was used for z . As a result, the mean plume velocity was as large as $5 \text{ m/s} \pm 12\%$, representing a 95 % confidence interval.

Applying the mean plume velocity to calculate the Nu number in Eq. (5), the mean and RMS gas temperature were compared with the assumption that $U_g = 2 \text{ m/s}$. The results are listed in Table A.9 and plotted in Figure A.5. Compared with $U_g = 2 \text{ m/s}$, the mean gas temperature decreased less than 3 K ($\sim 0.2\%$ at $Z = 10\text{cm}$ to 60cm) and the variance increased about 1 %. The results show that the gas velocity has little impact on temperature correction, in agreement with Ref. [16].

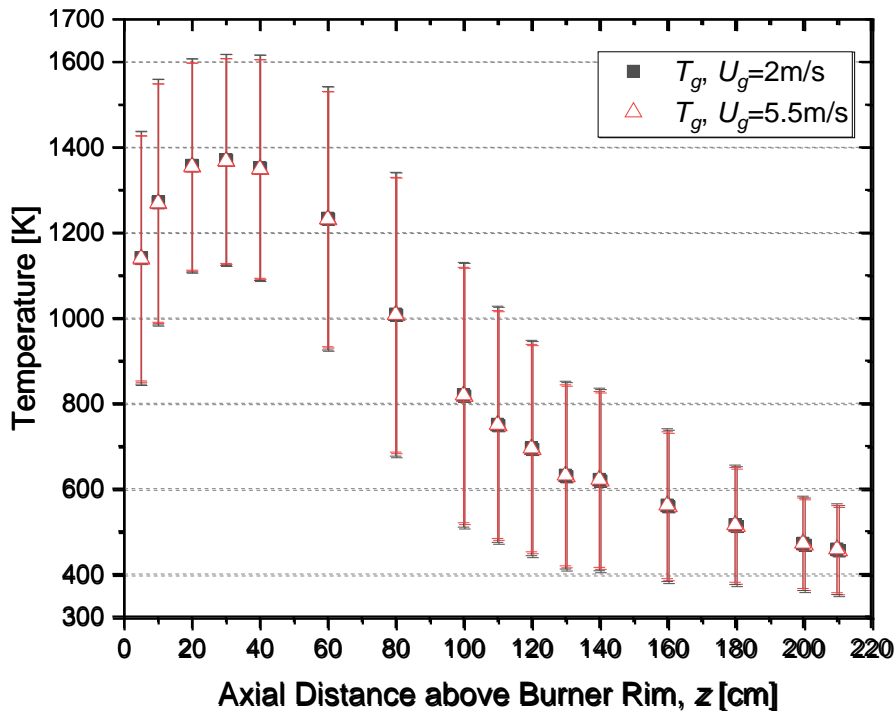


Figure A.5. Mean and variance of gas temperature as a function of the axial distance from the burner rim with $U_g = 2 \text{ m/s}$ and $U_g = 5.5 \text{ m/s}$.

Table A.9. Mean and variance gas temperature in the axial centerline of burner rim using $U_g = 2$ m/s and $U_g = 5.5$ m/s.

Z [cm]	$U_g = 2$ m/s			$U_g = 5.5$ m/s		
	T_g [K]	SD [K]	SD / T_g	T_g [K]	SD [K]	SD / T_g
5	1141	296	26%	1140	287	25%
10	1272	288	23%	1269	280	22%
20	1357	250	18%	1355	243	18%
30	1371	247	18%	1368	240	18%
40	1352	264	20%	1349	256	19%
60	1234	309	25%	1231	299	24%
80	1009	333	33%	1008	322	32%
100	820	310	38%	819	299	37%
110	751	277	37%	750	267	36%
120	695	252	36%	695	243	35%
130	631	220	35%	631	212	34%
140	621	214	34%	621	206	33%
160	561	179	32%	561	172	31%
180	515	140	27%	515	134	26%
200	472	111	23%	472	106	22%
210	458	106	23%	458	102	22%